Rayleigh Wave Attenuation and Amplification Measured at Ocean-Bottom Seismometer Arrays using Helmholtz Tomography

Joshua B. Russell[1], Colleen A. Dalton[1]

[1]Department of Earth, Environmental, and Planetary Sciences, Brown University, Providence, RI, USA

Corresponding author: Joshua B. Russell (joshua_russell@brown.edu)

Key Points:

- Helmholtz tomography applied at ocean-bottom seismometer arrays recovers Rayleigh wave attenuation and site amplification at 20–150 s period
- Synthetic tests show that focusing/defocusing are successfully accounted for, including near the coastline where strong multipathing occurs
- Strong site amplification observed at the Juan de Fuca ridge may be used to improve models of crust and shallow mantle

Abstract

Shear attenuation provides insights into the physical and chemical state of the upper mantle. Yet, observations of attenuation are infrequent in the oceans, despite recent proliferation of arrays of ocean-bottom seismometers (OBS). Studies of attenuation in marine environments must overcome unique challenges associated with strong oceanographic noise at the seafloor and data loss during OBS recovery in addition to untangling the competing influences of elastic focusing, local site amplification, and anelastic attenuation on surface-wave amplitudes. We apply Helmholtz tomography to OBS data to simultaneously resolve Rayleigh wave attenuation and site amplification at periods of 20–150 s. The approach explicitly accounts for elastic focusing and defocusing due to lateral velocity heterogeneity using wavefield curvature. We validate the approach using realistic wavefield simulations at the NoMelt Experiment and Juan de Fuca (JdF) plate, which represent endmember open-ocean and coastline-adjacent environments, respectively. Focusing corrections are successfully recovered at both OBS arrays, including at periods < 35 s at JdF where coastline effects result in strong multipathing. When applied to real data, our observations of Rayleigh wave attenuation at NoMelt and JdF revise previous estimates. At NoMelt, we observe a low attenuation lithospheric layer (Q_μ>1500) overlying a highly attenuating asthenospheric layer (Q_μ~50–70). At JdF, we find a broad peak in attenuation (Q_μ~50–60) centered at a depth of 100–130 km. We also report strong local site amplification at the JdF Ridge (>10% at 31 s period), which can be used to refine models of crust and shallow mantle structure.

Plain Language Summary

Seismic tomography provides a tool for probing regions deep within the Earth that are otherwise inaccessible. The degree to which seismic waves lose energy as they travel (seismic attenuation) provides information about temperature and melt in Earth's interior. However, seismic attenuation is notoriously difficult to measure due to complicating effects on wave amplitudes from focusing and amplification of the waves as they travel through the heterogeneous Earth. Here we introduce a tool that utilizes both amplitude and travel-time information observed across arrays of seismometers to account for these competing effects and accurately quantify seismic attenuation. We validate the approach using realistic synthetic data and apply it to real datasets at young (~3 Myr) and older (~70 Myr) locations in the Pacific Ocean. Our observations revise previous estimates of attenuation at the two locations, revealing high attenuation that extends deeper beneath the Juan de Fuca ridge than previously thought and high attenuation in the asthenosphere beneath the typical oceanic plate. These observations have important implications for our understanding of mantle temperature and melt content beneath the oceans.

1 Introduction

Shear attenuation of the upper mantle is a key parameter for quantifying the physical and chemical state of the asthenosphere. As attenuation and shear velocity respond differently to variations in temperature, melt fraction, grain size, and volatile content (Faul & Jackson, 2005; Jackson & Faul, 2010; McCarthy et al., 2011; McCarthy & Takei, 2011; Yamauchi & Takei, 2016), jointly interpreting these two observables offers unprecedented constraints on upper mantle properties (Dalton & Faul, 2010; Debayle et al., 2020; Havlin et al., 2021; Priestley & McKenzie, 2013; Richards et al., 2020). In contrast to shear velocity, which is routinely constrained at local and regional scales, our understanding of upper-mantle attenuation is largely limited to global models derived from Rayleigh wave observations (e.g., Adenis et al., 2017b, 2017a; Dalton et al., 2008; Karaoğlu & Romanowicz, 2018). This is especially true of the ocean basins where station coverage is sparse compared to the continents. In global models, shear attenuation beneath the ocean basins is primarily constrained by basin-traversing Rayleigh waves with long ray paths that tend to smear structure both laterally and vertically.

A primary challenge for all studies of Rayleigh wave attenuation is isolating the signal of attenuation in amplitude measurements from other effects, including source excitation, focusing/defocusing, and local site amplification. While progress has been made at longer periods at the global scale (e.g., Dalton & Ekström, 2006), the ability to robustly account for these effects at higher frequencies at regional and local scales is still a topic of active development (e.g., Forsyth & Li, 2005; F. C. Lin et al., 2012; Yang & Forsyth, 2006). Improving resolution of upper-mantle shear attenuation requires innovative seismic techniques that resolve regional-scale Rayleigh wave attenuation while accurately accounting for these additional factors that complicate wave amplitudes.

New surface-wave imaging techniques have been developed in recent years owing to an abundance of high-quality broadband seismic datasets with dense and uniform station coverage, such as the USArray. These techniques make use of the spatial gradients of Rayleigh wave amplitude and phase to extract structural information from the wavefield. Perhaps the most widely used to date is Helmholtz tomography, which yields regional-scale maps of phase velocity while accounting for finite-frequency effects (Jin & Gaherty, 2015; F.-C. Lin & Ritzwoller, 2011). The approach is attractive due to its simplicity compared to alternatives such as wave gradiometry (Langston, 2007a, 2007c, 2007b; Y. Liu & Holt, 2015) and requires fewer physical assumptions about the wavefield compared to simpler techniques such as the two-plane wave (TPW) method, which approximates the wavefield as the superposition of two plane waves with varying phase and amplitude (Forsyth & Li, 2005). Furthermore, the openly available Automated Surface-Wave Measurement System (ASWMS) software package has made Helmholtz tomography widely accessible to the seismology community (Jin & Gaherty, 2015). F. C. Lin et al. (2012) recently developed an extension of Helmholtz tomography for measuring Rayleigh wave attenuation and site amplification, which has been applied to USArray data (Bao et al., 2016; Bowden et al., 2017; F. C. Lin et al., 2012). However, it is not yet clear how effectively the technique can be applied at smaller scale arrays with often less optimal array geometries.

Despite recent methodological advances on land, seismic imaging in marine environments lags due to challenges associated with the relatively noisy seafloor environment and often sparse station coverage compared to terrestrial seismic deployments. This is true especially for studies of Rayleigh wave attenuation at ocean-bottom seismometer (OBS) arrays, where only a handful of observations have been made to date (e.g., Ma et al., 2020; Ruan et al., 2018; Saikia et al., 2021; Yang & Forsyth, 2006). To our knowledge, all existing regional Rayleigh wave attenuation observations made in the oceans were measured using the TPW method. While TPW provides a simple approach for measuring 1-D Rayleigh wave attenuation in the presence of weak or moderate multipathing, it may suffer in complex regions such as near the coastlines, where the wavefield may not be well approximated by two interfering plane waves. Furthermore, we are unaware of any previous reports of Rayleigh wave amplification in the oceans, despite having sensitivity to elastic structure that complements that of phase velocity (F. C. Lin et al., 2012; Schardong et al., 2019). Helmholtz tomography offers a promising approach that can simultaneously constrain attenuation and site amplification while accurately accounting for wavefield focusing/defocusing. However, it is unclear whether typical OBS array geometries and earthquake distributions offer the resolution needed for the technique to be successful as all previous applications have used well-behaved USArray data.

In this study, we show that Helmholtz tomography can be used to reliably measure Rayleigh wave attenuation and site amplification in oceanic settings, offering an alternative to the TPW method. We validate the approach using realistic wavefield simulations through 3-D elastic structure, demonstrating its ability to account for focusing/defocusing and recover attenuation and amplification. The methodology is applied at two OBS arrays representing endmember locales (open ocean and coastline adjacent) with apertures on the order of 500x500 km^2. Our observations revise previous estimates of Rayleigh wave attenuation at the two locations and provide perhaps the first measurements of site amplification in an oceanic setting. We implement the approach as an add-on to the ASWMS software, offering a new tool for estimating Rayleigh wave attenuation and amplification across regional-scale arrays that has been validated by realistic synthetic seismograms.

2 Data and Measurements

Broadband waveform data are utilized from the NoMelt Experiment and the Juan de Fuca (JdF) portion of the Cascadia Initiative, located in the central and eastern Pacific, respectively (Figure 1). The NoMelt experiment was positioned approximately 1200 km southeast of Hawaii on unperturbed, ~70 Ma seafloor far from hotspot, ridge, or subduction influences (P.-Y. P. Lin et al., 2016; Ma et al., 2020; Mark et al., 2019; Russell et al., 2019). The experiment consisted of a reflection/refraction survey (Mark et al., 2019), a magnetotelluric deployment (Sarafian et al., 2015), and a broadband OBS deployment from December 2012 to December 2013 (P.-Y. P. Lin et al., 2016; Ma et al., 2020; Mark et al., 2021; Russell et al., 2019). Here, we make use of the 16 broadband OBS with an array aperture of 400x600 km^2. Station depths range from 4889–5331 m.

The Cascadia Initiative was an amphibious experiment consisting of a multi-year broadband OBS deployment spanning the JdF and Gorda plates (Bell et al., 2016; Byrnes et al., 2017; Eilon & Forsyth, 2020; Hawley et al., 2016; Janiszewski et al., 2019; Ruan et al., 2018). We use data from the year 1 (23 stations; November 2011—May 2012) and year 3 (27 stations; August 2013—May 2014) deployments co-located on the JdF plate seaward of the trench. Here, water depth ranges from 2544 m to 2940 m. Stations in shallow water near the continental shelf are avoided due to noisier conditions and crust and mantle structure that is complicated by subduction processes (Janiszewski et al., 2019). While the majority of the 400x400 km^2 deployment footprint is characterized by nascent oceanic plate (~3 Ma average seafloor age), the JdF ridge cuts NNE-SSW across the western edge of the array.

The NoMelt and Juan de Fuca regions represent endmembers in terms of their seafloor age, structural complexity, and noise environment. The NoMelt experiment exemplifies an ideal OBS deployment for Rayleigh wave imaging. Its location in the center of the plate provides excellent azimuthal coverage for teleseismic Rayleigh waves, and the deep (>5000 m depth) open-ocean environment offers relatively quiet noise conditions. As most paths from source to receiver consist of largely homogeneous oceanic material, most arriving Rayleigh waves show little to no evidence of multipathing (Ma et al., 2020). In contrast, JdF represents a more challenging coastal environment. The region is characterized by shallower water depths (~2700

m) with higher noise levels and has azimuthal gaps in teleseismic earthquakes to the south and northeast. Additionally, large lateral gradients in velocity structure associated with the continent-ocean transition can produce complex Rayleigh waveforms exhibiting multipathing and scattering, particularly for waves traveling parallel to the coastline (Bell et al., 2016). These differences between the two focus sites allow us to test the limitations of the imaging approach.

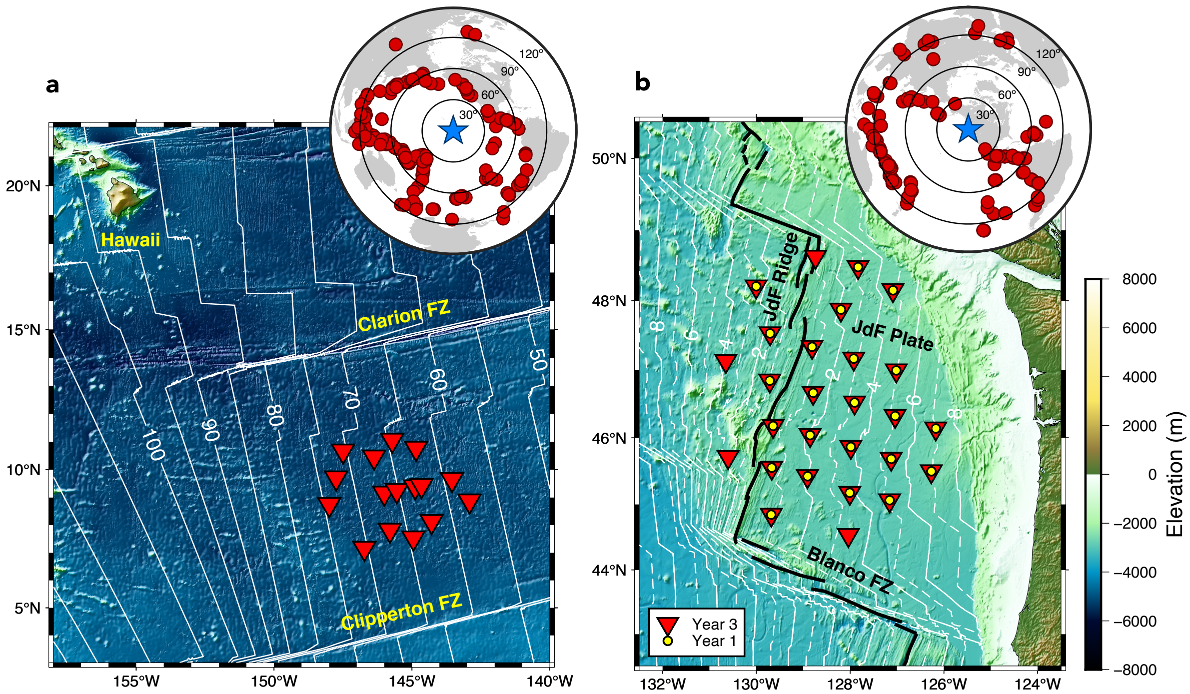

Figure 1. Maps of the (a) NoMelt experiment and (b) Juan de Fuca (JdF) component of the Cascadia Initiative. Event locations are shown at the top right of each panel. Seafloor age contours (white; labels in Myr) are from Seton et al. (2020). FZ = fracture zone

We retrieve four-component (3 directional and pressure-gauge) data for earthquakes in the Global Centroid Moment Tensor (GCMT) catalogue (Ekström et al., 2012) with $M_W > 5.5$, depths < 50 km, and epicentral distances ranging from 20º to 100º. Events with epicentral distances > 100º are avoided as they are more likely to have complicated paths (i.e., large portions that pass through continents), and phase and amplitude measurements for distances > 120º can be contaminated by major arc overtones (Hariharan et al., 2020). Although fundamental-mode Rayleigh wave excitation typically peaks at depths < 50 km, our dataset could be expanded in the future by considering deeper (primarily vertical dip-slip) earthquakes with considerable excitation below 50 km (Hariharan et al., 2022). As a rough initial quality control metric, we consider only events for which the vertical component Rayleigh wave appears at more than 5 stations with a signal-to-noise ratio (SNR) > 3 in the period band 20–80 s. In total, these criteria yielded 191 earthquakes for the NoMelt dataset and 160 earthquakes for JdF. That more events meet these criteria at NoMelt, which was deployed nearly half as long as JdF, is a largely a result of the lower noise levels at those stations.

2.1 Noise corrections

Vertical component OBS data is typically contaminated by tilt and compliance noise. Bottom-current noise typically contaminates the horizontal channels but can appear on the vertical channel as tilt noise if the instrument is slightly rotated from vertical (Crawford & Webb, 2000). Compliance noise results from long-period infragravity waves that produce pressure perturbations at the seafloor (Webb & Crawford, 1999). Both tilt and compliance noise typically dominate at periods > 80 s (depending on water depth) and therefore must be removed in order to make robust long-period surface-wave measurements. Tilt and compliance noise are removed from each vertical channel seismogram by applying the Automated Tilt and Compliance Removal (ATaCR) software package (Janiszewski et al., 2019). This tool employs the methodology developed by Crawford & Webb (2000) to estimate and remove coherent signals between the vertical and two horizontal channels and the vertical and pressure channel.

2.2 Phase and amplitude measurements

Rayleigh wave phase and amplitude are measured using the ASWMS software package, described in detail by Jin & Gaherty (2015). The tool employs a cross-correlation based approach to measure frequency-dependent interstation phase and group delay times and single-station amplitudes, and here we summarize the procedure. Each waveform is prefiltered using a second-order Butterworth filter with corner frequencies at ±25% of the maximum and minimum frequencies of interest. After prefiltering and windowing each seismogram around the Rayleigh wave arrival using an automated procedure, cross-correlations are calculated between all station pairs within each array. Cross-correlations with a correlation coefficient <0.65 are discarded. The remaining cross-correlation functions are narrow band filtered, and a five parameter Gaussian wavelet is fit at each frequency, yielding frequency-dependent interstation phase and group travel times, $\delta\tau_{ij}$ and $\delta\tau_{ij}^{g}$, for each station pair (i, j). Frequency-dependent amplitude measurements, A_i, are obtained at a single station by applying the same Gaussian wavelet fitting procedure to the autocorrelation function and taking the square root of the wavelet amplitude. This procedure is implemented in two overlapping frequency bands from 20–84 s and 73–150 s.

3 Methods

3.1 Helmholtz tomography

In its most common application, Helmholtz tomography (sometimes referred to as wavefront tracking) offers a method to solve for Rayleigh wave phase velocity maps, $c(x, y)$, from observations of phase delay, $\tau(x, y)$, and amplitude, $A(x, y)$ (Jin & Gaherty, 2015; F.-C. Lin & Ritzwoller, 2011). More recently, this technique has been extended for measuring Rayleigh wave attenuation and amplification at the USArray (Bao et al., 2016; F. C. Lin et al., 2012). Here, we briefly outline the main equations that govern the approach, relying heavily on the original derivation by F. C. Lin et al. (2012).

Consider a 2-D surface wave potential of the form $\chi(x, y, t) = A(x, y)\beta(x, y)^{-1} \exp\{i\omega(t - \tau(x, y))\}$. This surface-wave potential satisfies the 2-D homogeneous damped wave equation (Tromp & Dahlen, 1992) and balancing the real and imaginary parts yields the following two equations, respectively:

$$\frac{1}{c(x,y)^2} = \frac{1}{c'(x,y)^2} - \frac{\nabla^2(A(x,y)/\beta(x,y))}{\omega^2(A(x,y)/\beta(x,y))} \tag{1}$$

$$\underbrace{2\nabla\tau(x,y)\cdot\frac{\nabla\beta(x,y)}{\beta(x,y)}}_{\text{local amplification gradient}} - \underbrace{\frac{2\alpha(x,y)}{c(x,y)}}_{\text{anelastic attenuation term}} = \overbrace{\underbrace{2\nabla\tau(x,y)\cdot\frac{\nabla A(x,y)}{A(x,y)}}_{\text{apparent amplitude decay}} + \underbrace{\nabla^2\tau(x,y)}_{\text{focusing correction}}}^{\text{corrected amplitude decay}} \tag{2}$$

where ω is angular frequency, $c'(x,y) = |\nabla\tau(x,y)|^{-1}$ is apparent phase velocity, $c(x,y)$ is structural phase velocity, $\alpha(x,y)$ is the anelastic attenuation coefficient, and $\beta(x,y)$ is relative local site amplification of the surface-wave potential. For brevity, we drop the dependence on position (x,y) for the remainder of this manuscript. The anelastic attenuation parameter α is related to Rayleigh wave attenuation, Q^{-1}, by $\alpha = \omega/2CQ$, where C is group velocity. Because attenuation varies more strongly than group velocity, spatial variations in α should mostly reflect variations in Q^{-1}. Local amplification, β, is a relative measure of local amplitude and is sensitive to depth-dependent elastic structure at the receiver. Values of $\beta > 1$ indicate wave amplification and values of $\beta < 1$ correspond to wave deamplification. As pointed out by Bowden et al. (2017), β represents amplification of the surface-wave potential, which is not directly observable, and therefore it is not strictly equivalent to site amplification determined from more direct methods derived from amplitude ratios (e.g., Eddy & Ekström, 2014, 2020). The two quantities can be related via phase velocity through the expression $A_R/A_{R,0} = \beta\sqrt{c/c_0}$, where A_R is the Rayleigh wave amplification observed at a receiver of interest compared to a reference location $A_{R,0}$, and c/c_0 is the fractional difference in phase velocity relative to the value at the reference location.

Equation (1) with $\beta = 1$ is commonly referred to as the Helmholtz equation and can be used to solve for the structural phase velocity, c, given observations of τ and A (F.-C. Lin & Ritzwoller, 2011). The second term on the right-hand side that includes the Laplacian of the amplitude field normalized by ω^2 accounts for finite-frequency effects. In the high-frequency limit (i.e., ray theory), this term becomes negligible, and equation (1) reduces to the Eikonal equation (F.-C. Lin et al., 2009). For the purposes of this study, we assume $\beta = 1$ when solving equation (1) but not when solving equation (2).

Equation (2) is sometimes referred to as the transport equation and connects unknown quantities β and α on the left-hand side to spatial derivatives of measurable quantities τ and A on the right-hand side. Following the nomenclature of F. C. Lin et al. (2012), the first term on the right-hand side of equation (2) is the "apparent amplitude decay" in the direction of wave propagation and the second term consisting of the Laplacian of travel time is the "focusing correction". The entire right-hand side is referred to as the "corrected amplitude decay". On the left-hand side, we refer to the first and second terms as the "local amplification gradient" and "anelastic attenuation term", respectively.

Measured surface-wave amplitudes $A(\omega)$ include contributions from earthquake source excitation A_S, local receiver effects A_R, elastic focusing A_F, and amplitude decay due to anelastic attenuation along the ray path A_Q (Dalton & Ekström, 2006):

$$A(\omega) = A_S(\omega)\, A_R(\omega)\, A_F(\omega)\, A_Q(\omega) \tag{2}$$

Isolating the contribution from anelastic attenuation is the primary concern of all attenuation tomography, and here we describe how our methodology is able to do so. The receiver term, A_R, includes contributions from instrument response, tilt and compliance noise, and local site amplification. The former two contributions are removed prior to making measurements by deconvolving instrument response to displacement and subtracting tilt and compliance noise as described in Section 2.1, respectively. On the other hand, local site amplification, β, that results from energy amplification or deamplification due to elastic structure beneath the receiver, is solved for simultaneously alongside anelastic attenuation. Any imperfections in the instrument response and/or tilt and compliance removal steps at individual stations will map into site amplification and should not greatly affect attenuation.

Elastic focusing and defocusing, A_F, describes horizontal refraction of the wavefield and occurs due to lateral gradients in wavespeed in the Earth. Focusing and defocusing is especially prevalent near the coastlines, where large velocity gradients often exist (e.g., Russell & Gaherty, 2021). This behavior is reflected in the wavefield curvature and is accounted for by the focusing correction term, $\nabla^2\tau$, in equation (2). However, the $\nabla^2\tau$ term also includes simple geometrical spreading of the 2-D surface-wave wavefield, which results in defocusing and focusing at distances <90º and >90º, respectively, and can be expressed analytically as (see Supplementary Information; Text S1; Figure S2)

$$\nabla^2\tau_{GS} = \frac{\cos X}{cR\sin X} \tag{4}$$

where X is epicentral distance in degrees and R is Earth's radius. Therefore, amplitude focusing due only to structural heterogeneity along the ray path is given by $\nabla^2\tau - \nabla^2\tau_{GS}$.

The source term, A_S, includes azimuthal variations in Rayleigh wave amplitude associated with the radiation pattern. Surface waves emitted near nodes in the radiation pattern should be avoided as excitation is both weak and varies rapidly with azimuth. However, this bias has only a small effect on our amplitude dataset for three main reasons. First, the required SNR > 3 implicitly removes nodal events from our dataset. Second, the relatively small ~500x500 km^2 array footprint corresponds to only a small azimuthal range for a given teleseismic earthquake. Indeed, even at the larger USArray, Bao et al. (2016) found this bias to be small compared to other sources of error. Third, the governing equation (2) depends on the amplitude variation in the direction of propagation (i.e., the dot product on the right-hand side), whereas the radiation pattern introduces amplitude variations perpendicular to the propagation direction. We tested restricting our dataset to source excitation ratios >60% of the maximum to explicitly avoid nodes, but we observed no significant improvement (see Supplementary Figure S3), and a significant portion of the dataset was lost (~50–60% of events) degrading azimuthal coverage. For these reasons, we do not explicitly account for source excitation.

3.2 Solving for attenuation and site amplification

The local amplification gradient (first term in equation (2)) depends on propagation azimuth via the dot product with $\nabla\tau$, while the attenuation term containing α is independent of azimuth. To solve for the attenuation coefficient α and amplification β, we follow the curve-fitting approach of Bao et al. (2016). The local amplification gradient term can be expanded as

$$2|\nabla\tau|\left|\frac{\nabla\beta}{\beta}\right|\cos(\theta-\psi_\beta) = 2|\nabla\tau|\left(\,\partial_x(\ln\beta)\,\sin\theta + \partial_y(\ln\beta)\,\cos\theta\,\right) \tag{5}$$

where θ is the azimuth of wave propagation determined by $\theta = \tan^{-1}(\partial_x\tau/\partial_y\tau)$, and shorthand is used for spatial derivatives: $\partial_x = \partial/\partial x$, $\partial_y = \partial/\partial y$. The magnitude and azimuth of the local amplification gradient are given by $\left|\frac{\nabla\beta}{\beta}\right| = \sqrt{\partial_x(\ln\beta)^2 + \partial_y(\ln\beta)^2}$ and $\psi_\beta = \tan^{-1}\left(\partial_x(\ln\beta)/\partial_y(\ln\beta)\right)$, respectively. Substituting equation (*5*) into equation (2), replacing $|\nabla\tau|$ with $1/c'$, and multiplying both sides by $-c/2$ yields the simplified expression:

$$\alpha - \gamma\left(\,\partial_x(\ln\beta)\,\sin\theta + \partial_y(\ln\beta)\,\cos\theta\,\right) = \underbrace{-\frac{c}{2}\left(2\nabla\tau\cdot\frac{\nabla A}{A} + \nabla^2\tau\right)}_{\text{apparent attenuation}} \tag{6}$$

where c is estimated from equation (1) and $\gamma = c/c'$ accounts for biases due to finite-frequency effects and is typically close to unity when averaged over many azimuths. The right-hand side of equation (*6*) is referred to as the "apparent attenuation" and is a measured quantity for each earthquake in our dataset. The left-hand side of equation (6) contains the desired structural parameters—attenuation and site amplification—common to all events.

Maps of apparent attenuation are measured on an evenly spaced grid with pixel dimensions 0.5º×0.5º. We use γ as an additional quality control parameter, removing pixels for a given event that exceed $\pm 10\%$. We also discard pixels for a given event with a measured propagation azimuth > 10º from the great-circle path. Least-squares inversion of equation (6) yields log amplification gradients, $\partial_x(\ln\beta)$ and $\partial_y(\ln\beta)$, and attenuation coefficient, α, at a given pixel. To ensure smooth, well constrained maps, we adopt a binning approach whereby data within 1.5º of a central pixel are gathered and binned within 20º non-overlapping azimuthal bins. The inverse standard deviation of measurements within each azimuthal bin is used to weight the least squares inversion. This procedure is repeated across the study region, producing smoothed 2-D maps of $\partial_x(\ln\beta)$, $\partial_y(\ln\beta)$, and α. In practice, we do not interpret 2-D variations in attenuation due to the small array geometries and uneven azimuthal coverage, and instead, we solve for an array-averaged α by gathering measurements from all pixels within the array and performing a single inversion.

The resulting maps of $\partial_x(\ln\beta)$ and $\partial_y(\ln\beta)$ are used to invert for $\ln\beta$ via the centered 2-D finite-difference formula. The approximate derivatives of log amplification at pixel (x_0, y_0) are given by

$$\partial_x(\ln \beta)\big|_{(x_0,y_0)} = \frac{\ln \beta_{(x_0+1,y_0)} - \ln \beta_{(x_0-1,y_0)}}{2\Delta_x} \tag{7}$$

$$\partial_y(\ln \beta)\big|_{(x_0,y_0)} = \frac{\ln \beta_{(x_0,y_0+1)} - \ln \beta_{(x_0,y_0-1)}}{2\Delta_y} \tag{8}$$

where Δ_x and Δ_y is the grid spacing in the x and y directions. The least-squares inversion is unable to recover absolute amplification, and instead, we solve for the relative amplification by requiring that the mean of all $(\ln \beta)$ values within the study region is zero. This is equivalent to ensuring that the average β is equal to one. Additional smoothing is imposed on $\ln \beta$ maps by requiring small second spatial derivatives, $\nabla^2(\ln \beta) \approx 0$.

3.3 Constructing the gradient and Laplacian fields

The gradient and Laplacian fields of amplitude and phase travel time are required to construct the apparent attenuation term and solve equation (6) for the attenuation coefficient and local site amplification. One approach for estimating these fields for a given earthquake is to first fit smooth surfaces to absolute phase and amplitude measurements recorded at individual stations and then calculate the spatial gradients of these surfaces using finite-difference operators (Chevrot & Lehujeur, 2022; F.-C. Lin et al., 2009; F.-C. Lin & Ritzwoller, 2011). Removal of outliers is an important step prior to the surface fitting procedure to avoid anomalies in the surface that can amplify upon differentiation. This point is especially crucial for the Laplacian, which requires twice differentiation. Various fitting and regularization approaches have been used such as minimum curvature surface fitting (Bao et al., 2016; F.-C. Lin et al., 2009; F.-C. Lin & Ritzwoller, 2011), smoothing splines, and splines in tension (Chevrot & Lehujeur, 2022). Each approach aims to regularize the interpolation procedure such that gradients are well behaved. While minimum curvature smoothing may be acceptable for Eikonal tomography (Chevrot & Lehujeur, 2022), this form of regularization tends to suppress the Laplacian fields required for Helmholtz tomography, limiting one's ability to account for finite-frequency ($\nabla^2 A$) and focusing/defocusing ($\nabla^2 \tau$) effects.

We adopt an alternative approach for dealing with these challenges; our main philosophy is to avoid applying direct numerical differentiation when possible. We adopt the ray tomography method of Jin & Gaherty (2015), which uses the many interstation travel-time measurements that were determined by cross-correlation to construct the phase slowness vector field, $\nabla\tau$, directly. Below, we show how this can also be extended to the amplitude field to solve for $\nabla A/A$. This approach is attractive for several reasons. First, it does not require fitting a surface to single-station observations, but instead makes use of many more interstation observations derived from cross-correlations and therefore should be less susceptible to noise from any individual measurement. Second, the gradient field is solved for directly meaning that its character (smoothness, curvature) can be easily controlled via constraint equations within the inversion. Third, only one derivative is needed to calculate the Laplacian field, versus two when surface-fitting is applied to single-station travel-time or amplitude measurements. Finally, formal uncertainties from the inversion procedure are propagated through each step to ensure the best quality measurements are being fit in equation (6) (see Supplementary Text S1 for error propagation equations). We find that this ray-tomography approach more reliably recovers input synthetic attenuation values compared to the surface fitting procedure in some cases (Figure S5).

The differential phase travel time between two stations i and j, $\delta\tau_{ij}$, is expressed as the path integral of the travel-time gradient (or phase slowness) along the great-circle connecting the stations. In practice, this equation is discretized, and we solve separately for the x and y components of the travel-time gradient:

$$\delta\tau_{ij} = \int_i^j \nabla\tau \cdot dr \approx \sum_{k=i}^{j} \partial_x\tau_k \cdot dx_k + \partial_y\tau_k \cdot dy_k \tag{9}$$

where dx_k is the path length through the kth cell projected onto the x-direction with an equivalent definition for dy_k. After solving for the x and y components of the travel-time gradient, dynamic phase velocity maps are calculated from $c' = \left[(\partial_x\tau)^2 + (\partial_y\tau)^2\right]^{-1/2}$, and the focusing corrections are given by $\nabla^2\tau = \partial_x(\partial_x\tau) + \partial_y(\partial_y\tau)$. We perform an analogous inversion of group travel-times, $\delta\tau_{ij}^{g}$, for maps of group velocity C, allowing for the estimation of Rayleigh wave attenuation via $Q^{-1} = 2C\alpha/\omega$.

The inverse problem for the x and y components of the gradient field is solved using a least-squares approach with a second derivative smoothing (i.e., minimum curvature) constraint (Jin & Gaherty, 2015). The smoothing operator is rotated to the local radial and transverse directions at each grid cell (assuming great-circle propagation) and a solution is found that minimizes the following penalty function:

$$E = \sum \left| \delta\tau_{ij} - \int_i^j \nabla\tau \cdot dr \right|^2 + \frac{\varepsilon\lambda}{\Delta} \sum \{ |\nabla^2(\partial_R\tau)|^2 + |\nabla^2(\partial_T\tau)|^2 \} \tag{10}$$

where $\partial_R\tau$ and $\partial_T\tau$ are the phase slowness parallel and perpendicular to the great-circle path, respectively. The first sum is over all inter-station travel times, and the second sum is over all grid cells. To impose frequency-dependent smoothing, we weight the smoothing constraint by the ratio of approximate wavelength-to-grid spacing, λ/Δ. The global smoothing parameter, ε, is used to balance the relative importance of data fit and model roughness, and we choose a moderate value of 0.1. For our chosen grid spacing of 0.5º×0.5º, this results in overall smoothing weights that range from 0.14 at a period of 20s to 1.1 at 150 s.

Because we solve for the gradient field directly, the second derivative smoothing constraint in equation (10) is equivalent to minimizing the third spatial derivative of travel time, $\nabla^3\tau$. This requires that the Laplacian field smoothly varies. While this may limit our ability to resolve sharp gradients in the focusing term, $\nabla^2\tau$, it provides a robust solution given the finite set of unevenly distributed observations. We choose not to apply a first derivative smoothing constraint in the inversion as this would enforce propagation along a great-circle arc, resulting in a focusing correction term that perfectly captures the effects of geometrical spreading but does not account for elastic focusing and defocusing due to lateral velocity gradients.

We use an analogous approach to solve for the normalized amplitude gradient field $\nabla A/A$ found in equation (6). Because our amplitude measurements are single-station values, we first form the log amplitude difference between a pair of stations, $\delta \ln A_{ij} = \ln A_i - \ln A_j$, and then relate it to the x and y components of the gradient field using

$$\delta \ln A_{ij} = \int_i^j \frac{\nabla A}{A} \cdot dr \approx \sum_{k=i}^{j} \frac{\partial_x A_k}{A_k} \cdot dx_k + \frac{\partial_y A_k}{A_k} \cdot dy_k \tag{11}$$

This expression is inverted via least squares by minimizing the penalty function analogous to equation (10). With maps of $(\partial_x A/A\,, \partial_y A/A)$ and $(\partial_x \tau\,, \partial_y \tau)$ for each earthquake, we calculate the amplitude gradient along the direction of propagation, $\nabla\tau \cdot \nabla A/A$, and construct the apparent attenuation term (i.e., the right-hand side of equation (6)) and solve for α and β following Section 3.2.

4 Synthetic Wavefield Simulations

While the Helmholtz technique has been successfully applied at the USArray for measuring Rayleigh wave attenuation and site amplification (Bao et al., 2016; F. C. Lin et al., 2012), it has not yet been applied at an OBS array. In contrast to USArray's uniform ~70 km station spacing, a typical OBS experiment comprises a smaller footprint with often uneven station coverage due to chosen experiment geometry and/or data loss, making it more difficult to accurately recover the gradient and Laplacian fields. Experiments near the continental shelf, such as JdF, represent an especially challenging setting as strong focusing and amplification are expected to occur due to the abrupt velocity contrast at the ocean-continent transition. Additionally, conditions on the seafloor are often noisier than on land, affecting the quality of travel-time and amplitude measurements. Each of these factors contribute to difficulties associated with measuring intrinsic Rayleigh wave attenuation in the ocean basins. To test some of these limitations and validate the approach, we apply the methodology outlined in Section 3 to a realistic synthetic dataset comprising the real station and event geometry. This also provides an opportunity to compare the Helmholtz approach with the two-plane-wave approach (Forsyth & Li, 2005; Yang & Forsyth, 2006), which has been used to measure attenuation at several OBS arrays (e.g., Ruan et al., 2018; Yang & Forsyth, 2006), in a self-consistent manner.

We generate synthetic seismograms for all of the same events and stations used in the real dataset for both the NoMelt and JdF experiments using the SPECFEM3D GLOBE software (Komatitsch & Tromp, 2002b, 2002a). This includes simulations for 160 earthquakes for JdF and 191 at NoMelt. The 3-D elastic model used for the simulations consists of CRUST2.0 (Bassin et al., 2000) overlying the mantle model S362ANI (Kustowski et al., 2008), and attenuation is specified by 1-D model QL6 (Durek & Ekström, 1996). Hereafter, we refer to the full 3-D model as S362ANI+CRUST2.0 (Figure 2). The mesh is constructed such that 832 spectral elements lie along a great circle, resulting in an average spectral element width of ~48 km and a minimum resolved period of ~20 s.

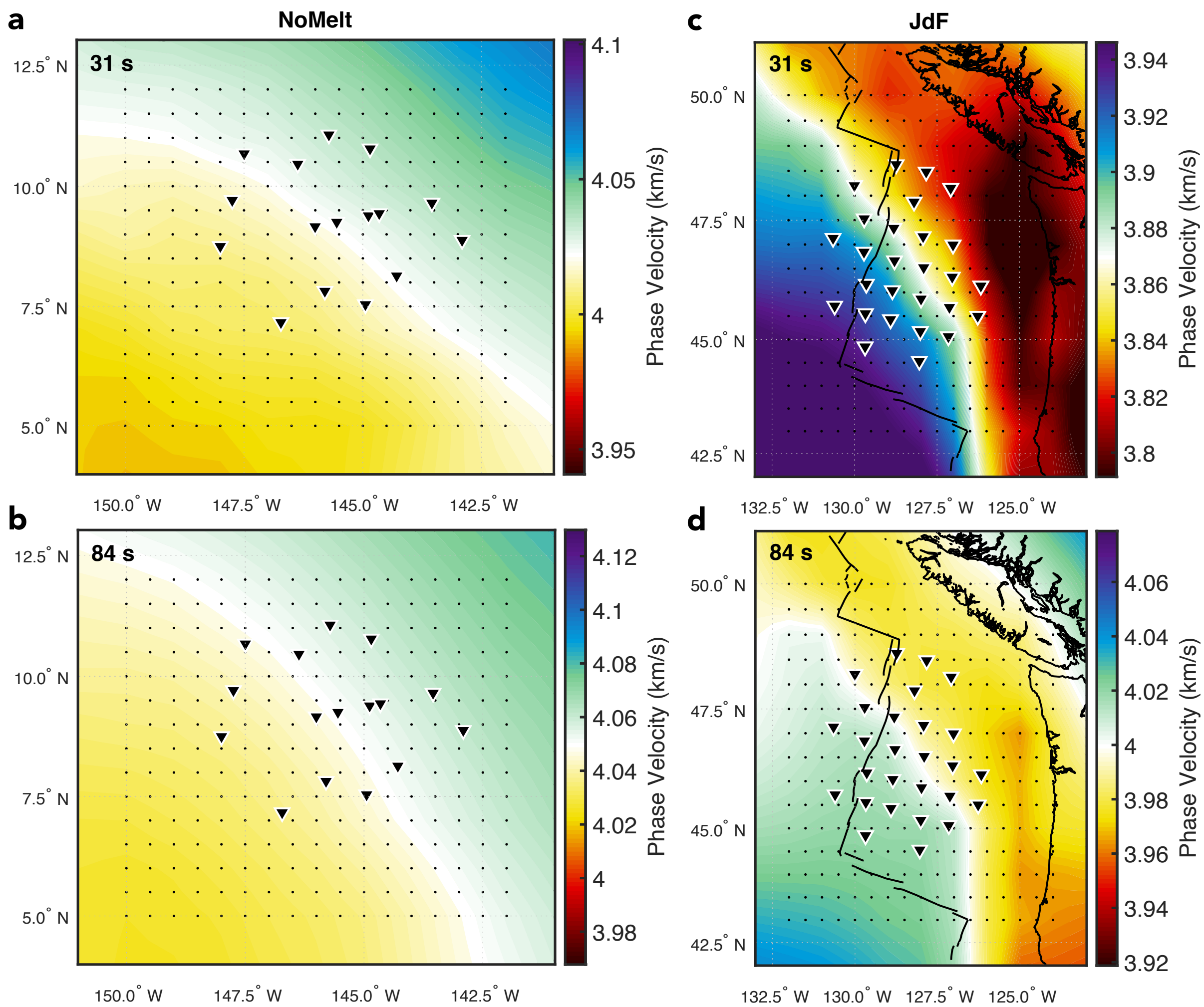

Figure 2. Synthetic phase velocity maps for 3-D global mantle model S362ANI (Kustowski et al., 2008) combined with CRUST2.0 (Bassin et al., 2000) at (a,c) 31 s and (b,d) 84 s period. Phase velocities were estimated every 1º using MINEOS. (left) NoMelt and (right) JdF station geometries are indicated by black triangles. The finely spaced (0.5º×0.5º) black points show the locations at which the SPECFEM3D GLOBE synthetic wavefield was sampled for idealized synthetic testing in Figure 3a–c; this sampling interval is approximately equal to one spectral element and corresponds to the grid spacing used in the ray tomographic inversion for the gradient fields. Colors range from -2% to +2% about the mean velocity. Maps are corrected for physical dispersion using the 1-D model QL6 (Durek & Ekström, 1996) and a reference frequency of 1 Hz.

The synthetic seismograms include realistic effects on Rayleigh wave phase and amplitude caused by wavefield focusing, defocusing, and scattering due to 3-D elastic heterogeneity, intrinsic attenuation, local site amplification, finite-frequency effects, and overtone interference. In addition to calculating seismograms at the true station locations, we also sample the wavefield on an evenly spaced 0.5ºx0.5º grid over a broader region centered on each array (black points in Figure 2). This idealized geometry should allow us to more accurately recover the true gradient and Laplacian fields, providing a benchmark for assessing how well those fields are estimated using the true station geometries. The procedures used to measure phase and amplitude and invert for gradient and Laplacian fields for the synthetic dataset are identical to those used for the real data.

NoMelt and JdF represent endmember locations in terms of structural complexity. Figure 2 shows phase velocity maps at 31 s and 84 s period for S362ANI+CRUST2.0 estimated by sampling 1-D profiles from the 3-D model at 1º intervals and applying MINEOS to calculate Rayleigh wave dispersion. The maps have been corrected for the effect of physical dispersion using a reference frequency of 1 Hz (H. Liu et al., 1976). There is a clear contrast between NoMelt and JdF, particularly at 31 s period, for which phase velocities vary by more than ±2% at JdF but are typically <0.5% at NoMelt. We note that slow velocities associated with the JdF Ridge (e.g., Bell et al., 2016) are absent from the coarse 3-D model. Regardless, the sharp velocity contrast in the region associated with the continent-ocean transition still allows us to test the limitations of the methodology.

5 Results

5.1 Focusing corrections

Figure 3 shows example maps of apparent amplitude decay, focusing correction, and corrected amplitude decay for a Mw 6.4 earthquake originating at the southern East Pacific Rise and propagating north-northwest across the JdF array. The propagation direction approximately parallels the coastline, representing an extreme case of focusing and defocusing that manifests as strong NW-SE banding in the amplitude decay maps parallel to the direction of wave propagation (Figure 3a,d,g). Three main observations can be made: First, the focusing effects are significant and greatly impact the amplitude decay field (Figure 3a–c). Second, the true station geometry is sufficient for resolving the focusing correction term and, in turn, the corrected amplitude decay field (Figure 3d–f). Third, the data show a similar overall behavior to the synthetic measurements, indicating that even in the noisy seafloor environment focusing effects can be observed and corrected for (Figure 3g–i).

The amplitude decay (Figure 3a,d,g) and focusing correction terms (Figure 3b,e,h) display similar patterns that are opposite in sign such that the coastline-parallel banding is significantly reduced when added together to form the corrected amplitude decay map (Figure 3c,f,i). For this event, the sign of the strongest focusing correction is positive (blue) indicating *defocusing* of the wavefield. In other words, wave amplitudes in the blue regions of Figure 3b,e,h decay more strongly than dictated by intrinsic attenuation, and thus, failing to correct for defocusing would result in attenuation estimates that are biased high at those pixels for this event. In contrast, the region of strong amplitude decay (red) near the coastline in Figure 3a is not removed by the focusing correction and therefore is likely related to site deamplification as waves propagate from the continent into the ocean. The slightly positive regions at the edges of the corrected amplitude decay maps (Figure 3f,i) are likely artifacts due to edge effects in the gradient and/or Laplacian estimates. Because we consider many events from various azimuths, such edge effects do not strongly bias estimates of attenuation or site amplification.

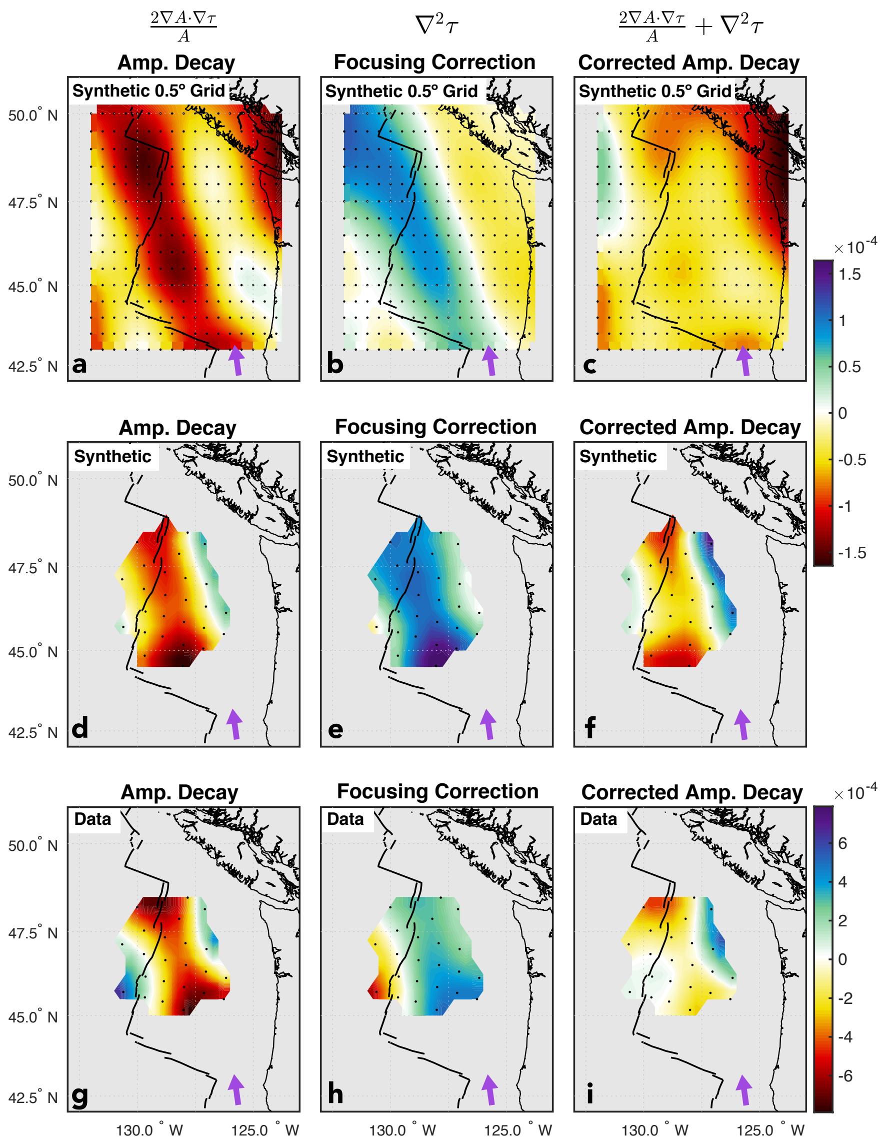

Figure 3. Demonstration of the 55 s period focusing/defocusing correction at JdF for a Mw 6.4 strike-slip earthquake that occurred at the southern East Pacific Rise on May 12, 2014 (13:58:21.5 GMT). Maps of (a) apparent amplitude decay, (b) focusing correction, and (c) corrected amplitude decay estimated from SPECFEM3D GLOBE synthetics for idealized station spacing of 0.5º×0.5º. Black points indicate station/sampling locations from Figure 2. The purple arrow shows the direction of wave propagation. (d–f) Same as a–c but for SPECFEM3D GLOBE synthetics sampled at the true OBS locations. (g–i) Same as d–f but for the real observations. Note the larger range of values in g–i.

The resemblance between the synthetic and observed focusing corrections in Figure 3 is remarkable given the high noise levels typically associated with OBS data and suggests that the velocity structure of S362ANI+CRUST2.0 between this particular source and receiver (see Supplementary Figure S1) resembles the true structure at 55 s period. However, the maximum amplitude of the focusing corrections for the real data is larger by a factor of ~5, likely due to the global model being smooth, which reduces the overall amplitude of focusing and defocusing.

We further explore the focusing corrections by investigating their distribution for all events in the catalogue at both NoMelt and JdF (Figure 4), after removing the effects of geometrical spreading via equation (4). The resulting "structural focusing correction" should reflect focusing/defocusing due to lateral variations in wavespeed along the ray path, both prior to the Rayleigh wave entering the array as well as within the array footprint. The distributions of focusing corrections at NoMelt are narrow, strongly peaked around zero, and relatively symmetric for both data and synthetic, while at JdF they are more broadly distributed. This is due to the stronger velocity gradients present at JdF compared to NoMelt (Figure 2). In addition, the distribution at 31 s period is skewed from zero at JdF, and this skew in the data occurs in the opposite sense from the synthetic. A negative skew in the real data indicates a tendency for the wavefield to be focused upon entering the array, while a positive skew in the synthetic data indicates defocusing. This difference can be understood by considering the vastly different velocity structure in the western region of the array for data and synthetic (Figure 4c,f), together with the strongly biased event distribution (Figure 4g) with most events arriving from the west. Waves entering the array from the west in the real Earth are preferentially focused by the slow velocities (< 3.7 km/s at 31 s period) along the JdF Ridge (Figure 4f), while waves from those same events in the synthetic model are defocused by the fast oceanic plate velocities to the west (Figure 4c). Again, the focusing corrections for the real data are 4–5 times larger than for the synthetics. This is true at both locations and for 31 s and 84 s period.

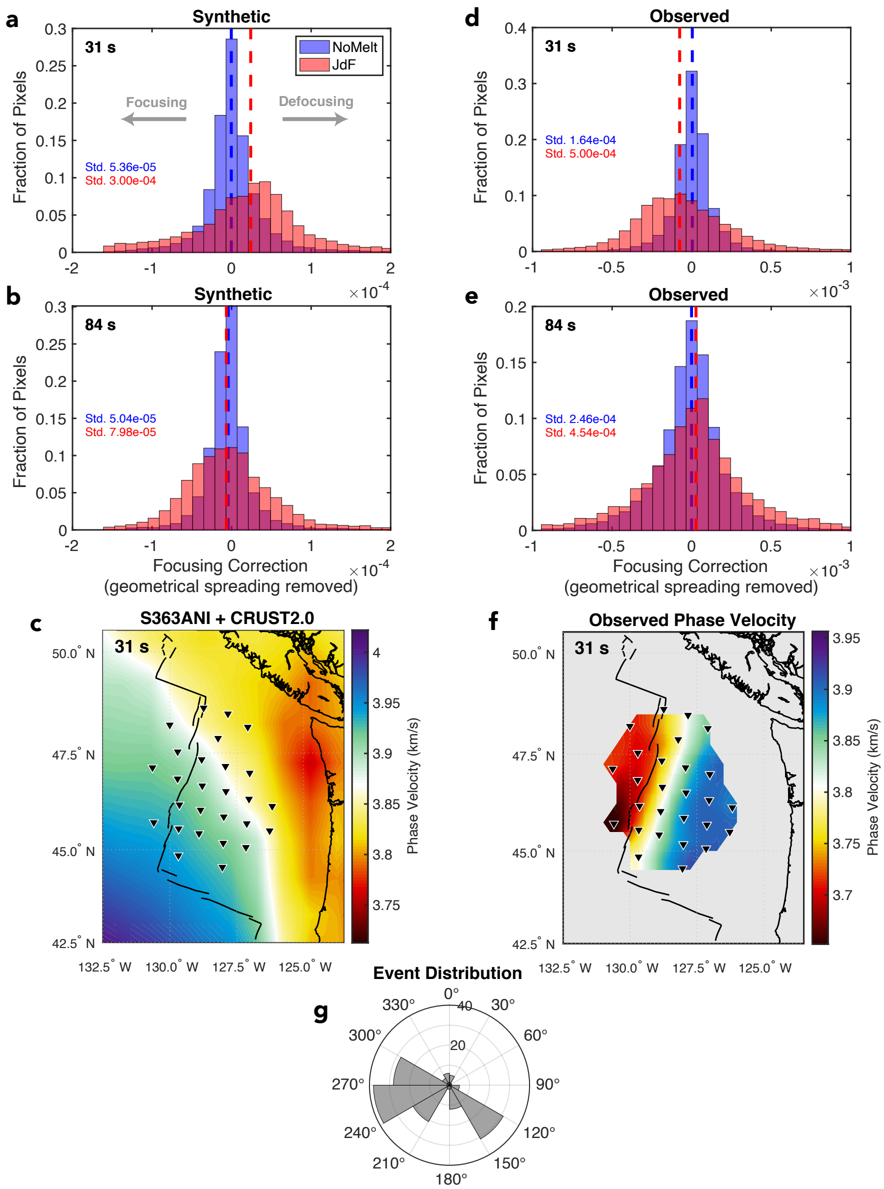

Figure 4. Distribution of structural focusing corrections at NoMelt (blue) and JdF (red) at (a) 31 s and (b) 84 s period for the synthetic dataset using the true station geometries (left) and real observations (right). The effect of geometrical spreading has been removed via equation (4), and therefore wave focusing (negative values) and defocusing (positive values) are due to lateral variations in wavespeed along the propagation path. Vertical dashed lines show the median values of the distributions. (c) Synthetic phase velocity map at 31 s period for reference. (d–f) Same as a–c but for the real observations. (g) Distribution of earthquake back azimuths at JdF, indicating most events originate from the west. Synthetic and observed focusing behavior is similar overall, except for JdF at 31 s period, where the skew in correction terms for the real observations indicates preferential focusing. This difference arises from the slow velocities along the western edge of the array associated with the JdF Ridge (f) — replaced by fast velocities in the synthetic model (c) — which focuses waves arriving from the west. Note the factor of 5 larger horizontal axis range in d,e compared to a,b.

5.2 Local site amplification

Amplification is estimated from the azimuthal variation of apparent attenuation (e.g., Figure 5a, Figure 6a) via equation (6). The minimum of the sinusoid corresponds to the azimuth of maximum Rayleigh wave amplification, $\beta > 1$ (likewise, the peak of the sinusoid indicates the azimuth of maximum deamplification, $\beta < 1$). For example, Figure 6a shows a minimum at ~60º for the synthetic JdF dataset, which indicates that waves traveling northeast across the array are preferentially amplified. This is reflected in the maps of β (Figure 6b). In this case, failing to account for amplification would result in an apparent $\alpha < 0$ for observations at this propagation azimuth (i.e., wave amplitudes *increase* with propagation distance). This demonstrates the importance of considering Rayleigh wave amplification and attenuation together as well as the need for decent azimuthal coverage, which is discussed further in Section 6.1.

We evaluate our ability to accurately recover site amplification using the realistic OBS array geometries. Local site amplification is predicted for the 3-D model S362ANI+CRUST2.0 at a desired pixel and frequency from the following expressions (F. C. Lin et al., 2012)

$$\beta(x, y, \omega) = \left(\frac{cCI}{\overline{cCI}}\right)^{-\frac{1}{2}} \tag{12}$$

$$I = \frac{1}{U(a)^2}\int_0^a \rho(r)(U(r)^2 + V(r)^2)r^2\,dr \tag{13}$$

where $\overline{cCI}$ is the average value within the array, therefore ensuring the mean of the predicted β maps equals one as prescribed by the inversion (see section 3.2), and U and V are the vertical and horizontal displacement eigenfunctions at position (x, y), respectively. The integral is carried out from Earth's center to the seafloor at radius a.

Relative amplification (β) is recovered successfully from the synthetic dataset at both NoMelt (Figure 5) and JdF (Figure 6) at periods of 31 s and 84 s using the real station geometries and event distributions. The correlation coefficient between measured and predicted values at both locations is > 0.95, except for at NoMelt at 31 s period (R = 0.788; Figure 5d) for which amplification and deamplification are weak (< 0.5%). Measured and predicted β maps at both locations are anti-correlated with the phase velocity maps shown in Figure 2, as expected (F. C. Lin et al., 2012). Regions of amplification and deamplification correspond to slow and fast phase velocities, respectively. Amplification at NoMelt is <1% due to the relatively modest velocity variations in S362ANI+CRUST2.0 at this location, whereas JdF shows up to 5–7% amplification at 31 s period due to the strong low velocities on the eastern edge of the array associated with the transition to continental crust.

The highest predicted values of amplification at JdF of ~1.07 are slightly underestimated by the measurement routine at ~1.05 (Figure 6d). This may be due to the strongest amplification in the northeast being located at the edge of the map where fewer data are available for binning within the surrounding 1.5º radius for the inversion. On the other hand, strong deamplification values ($\beta < 1$) at the southwest edge of the map are very well recovered. Another possibility is that a slight tradeoff exists between β and α due to the uneven azimuthal coverage (Figure 4g). Although our 20º azimuthal binning procedure should lessen such biases, azimuthal gaps inevitably exist for any given pixel in the map.

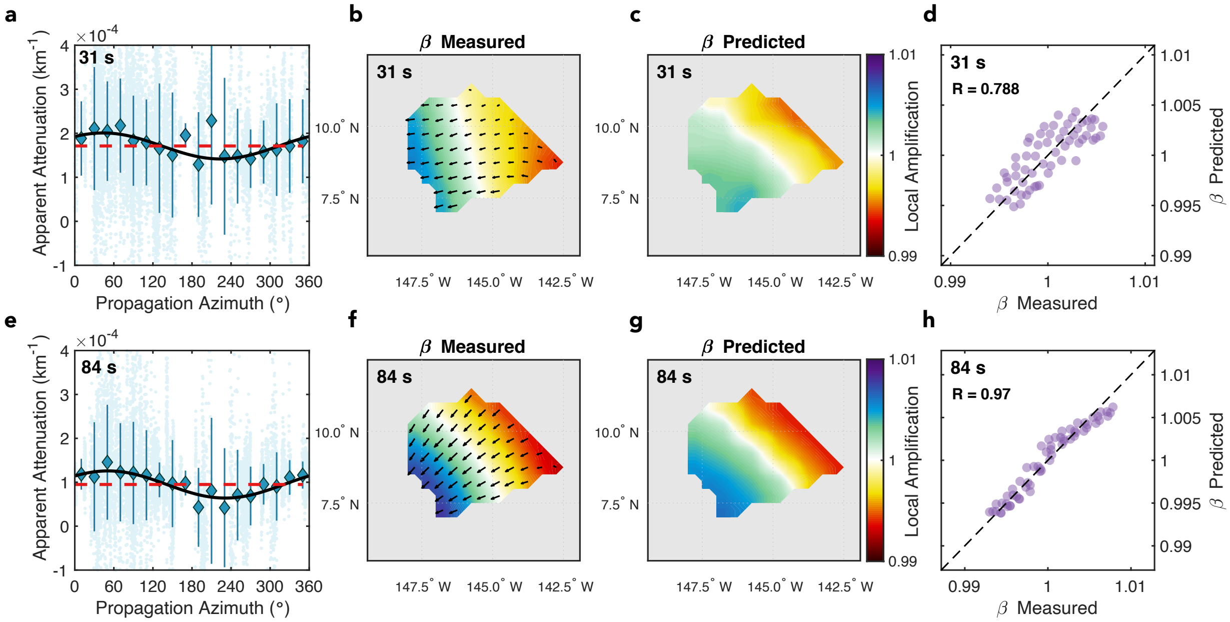

Figure 5. Synthetic recovery test of site amplification, β, at NoMelt. (a) Measurements of apparent attenuation (i.e., right-hand side of equation (6)) at 31 s period for all events and pixels. Blue diamonds and error bars show the mean and standard deviation of points within 20º azimuthal bins, and the best fitting 1-D sinusoid is shown in black. The red dashed line indicates the estimate of array average anelastic attenuation, α. To estimate lateral variations in amplification, we apply this same fitting procedure pixel-by-pixel (see Section 3.2 for details). (b) Recovered amplification maps via equations (7–8), where black vectors show the log amplification gradient at each pixel obtained by binning measurements within a 1.5º radius and performing fitting as in a). (c) Amplification predicted from the 3-D synthetic model S362ANI+CRUST2.0 using equations 12–13. (d) Comparison of measured and predicted amplification with correlation coefficient shown at the top left. (e–h) Same as a–d but for 84 s period. Both measured and predicted amplification maps are normalized such that the average within the array equals 1. Values of $\beta > 1$ correspond to amplification and $\beta < 1$ correspond to deamplification.

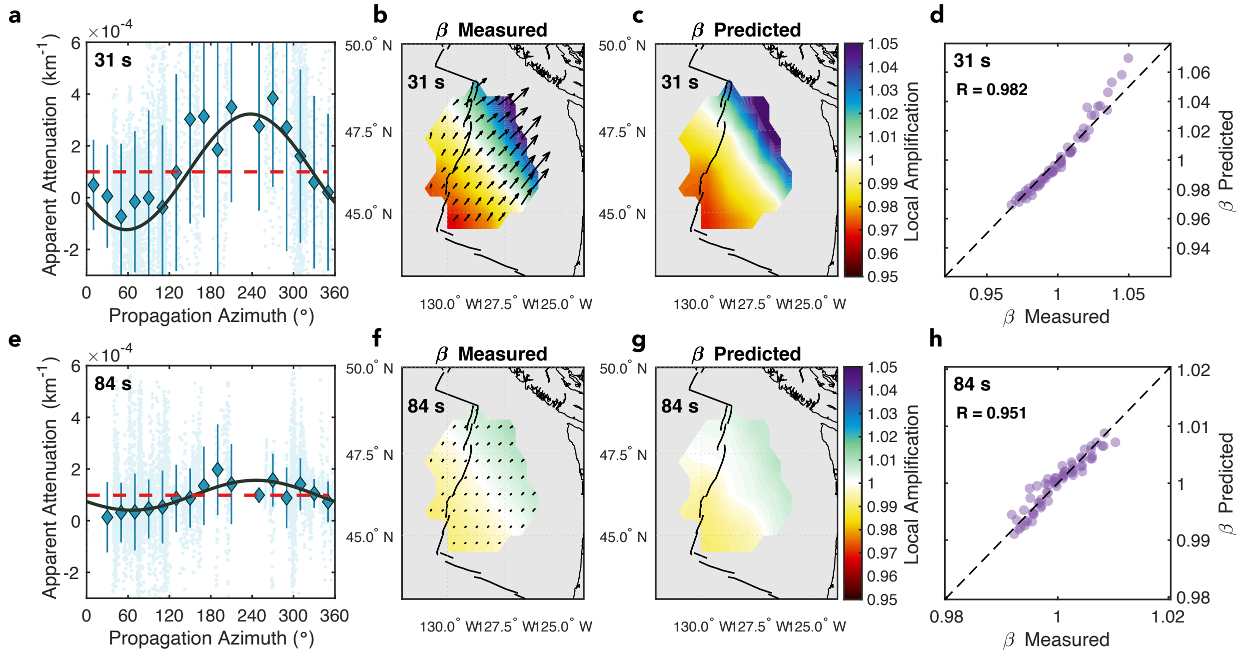

Figure 6. Synthetic recovery test of site amplification, β, at JdF. See Figure 5 caption for details.

The real observations reveal similar first order differences in β as the synthetics at NoMelt and JdF with overall weak amplification/deamplification at NoMelt (Figure 7a,b) and stronger values at JdF (Figure 7c,d). The observed amplification variations at NoMelt are less spatially coherent at the two periods of interest, likely because the magnitudes of amplification and deamplification at NoMelt are small (< 1%); indeed, the synthetic recovery tests demonstrate that weaker amplification variations are more difficult to resolve (Figure 5d). In contrast, β maps at JdF show strong variations in amplification (> 10% at 31 s period) that are spatially coherent at both periods of interest and correlate reasonably well with the low-velocity JdF Ridge (Figure 4f). These are among the first amplification maps observed in an oceanic setting and can be used together with complementary observations of Rayleigh wave phase velocity to better constrain shear and compressional velocities and density (e.g., Bowden et al., 2017; F. C. Lin et al., 2012), as discussed further in Section 6.3.

5.3 Rayleigh wave attenuation

With the synthetic data sets, we successfully recover the input 1-D Rayleigh wave attenuation at both NoMelt and JdF (Figure 8). We obtain 1-D estimates of attenuation by grouping all apparent attenuation measurements for the whole study area and solving for a single representative α (and $\nabla\beta/\beta$). Our implicit assumption that a single value of $\nabla\beta/\beta$ at each period can sufficiently represent the true variation in the maps in Figures 5 and 6 is reasonable given that β tends to vary smoothly (and simply) across our small study regions; violation of this assumption should result in larger α uncertainties. Uncertainties in the recovered α values are generally smaller at NoMelt likely owing to the weaker focusing and defocusing (Figure 4), weaker amplification variations (Figure 5), and better azimuthal coverage (Figure 1). Uncertainties at JdF are especially large for periods < 30–40 s indicating that the strong focusing and defocusing at these periods is not perfectly accounted for, even for the noise-free synthetic tests, likely due to the complex focusing patterns and difficulties resolving $\nabla^2\tau$ with sparse station coverage. It is possible that unaccounted for scattering attenuation due to the abrupt velocity changes at the coastline also contributes to these larger uncertainties. Nevertheless, the input attenuation values are recovered to within uncertainty at all periods from 20–150 s at both locations.

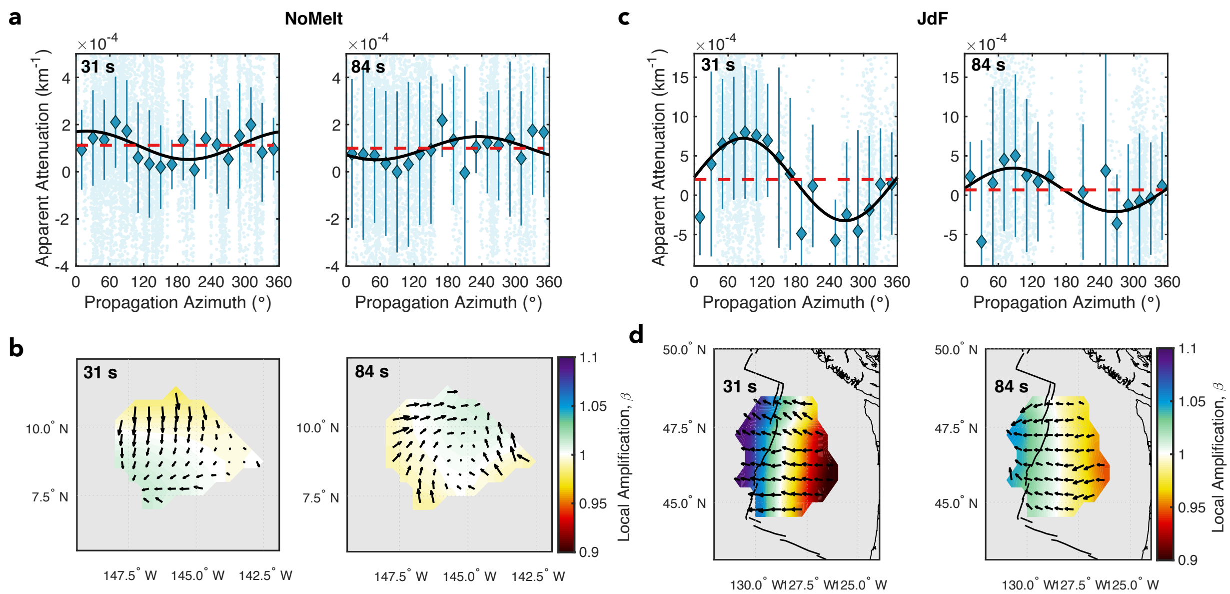

Figure 7. Amplification maps observed from the real datasets. (a) Apparent attenuation data (right-hand side of equation (6)) and (b) local amplification maps at NoMelt at 31 s and 84 s period. (c,d) Same as a,b but for JdF. Symbols as in Figures 5 & 6. Amplification maps are normalized by the array average value. Note the difference in the vertical axes in a) and c).

Attenuation recovered using the true station geometry (red symbols in Figure 8) agrees with values measured using the idealized 0.5º grid (blue symbols), albeit with larger uncertainties. The smaller uncertainties for the idealized station geometry likely reflect its ability to better recover the true focusing and defocusing corrections. However, for periods <35 s at JdF, uncertainties are large also for the idealized geometry indicating that the focusing correction terms are not perfectly resolved and could perhaps be improved with finer station spacing (< 0.5º) and/or a weaker second-derivative smoothing constraint. In addition, the idealized geometry encompasses a larger area, and therefore the assumption of 1-D $\nabla\beta/\beta$ is less valid, particularly at the shorter periods.

We compare our Helmholtz results with those of the TPW inversion (Forsyth & Li, 2005; Yang & Forsyth, 2006) applied to the same synthetic phase and amplitude dataset using the true station geometry (green symbols in Figure 8). Because the datasets are identical, differences between the TPW and Helmholtz results are entirely due to differences in the theoretical treatments of phase and amplitude. We find excellent agreement between Helmholtz and TPW at all periods at NoMelt and at periods > 40 s at JdF, where focusing and defocusing are relatively weak (Figure 4). For these scenarios, the wavefield can be sufficiently approximated by two interfering plane waves. However, at JdF large differences appear at periods < 35 s, where TPW is unable to recover the true 1-D attenuation within uncertainty. This breakdown of the TPW technique indicates that the complex wavefield focusing and defocusing near the coastline in the

S362ANI+CRUST2.0 model cannot be sufficiently described by the interference of two plane waves.

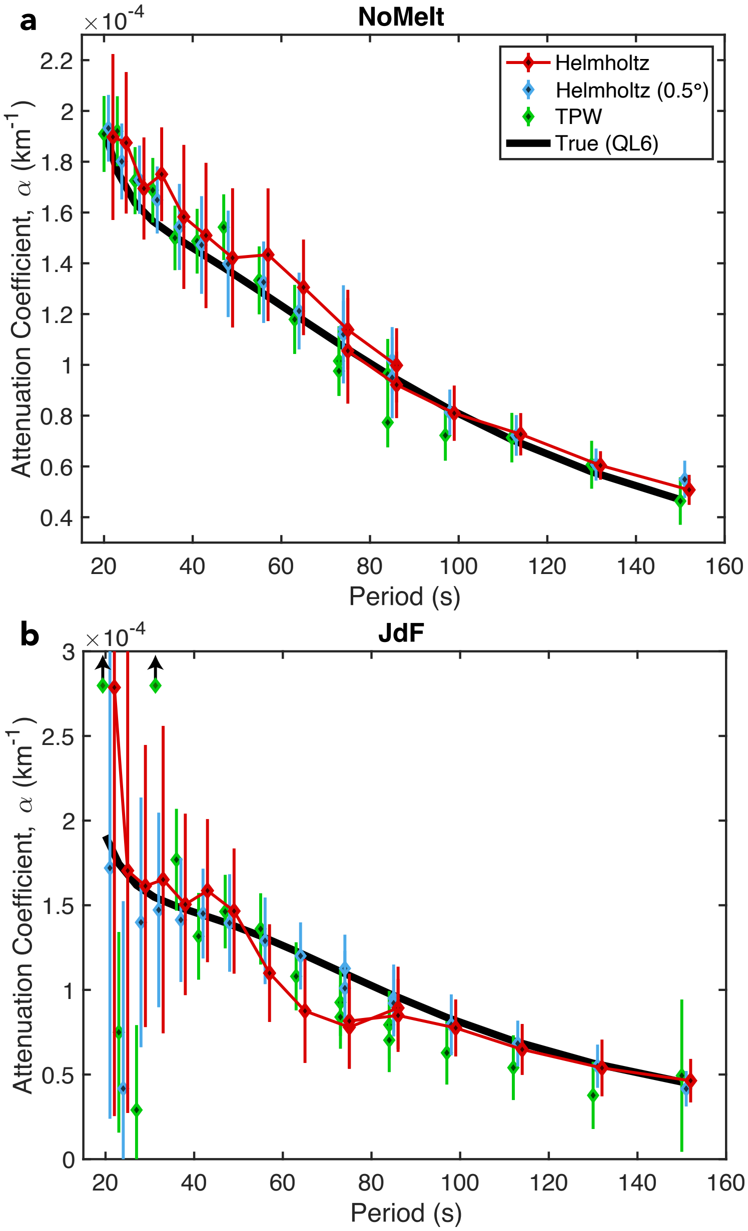

Figure 8. Recovery of synthetic 1-D attenuation coefficient, α, at (a) NoMelt and (b) JdF for periods of 20–150 s. The input attenuation values of QL6 (Durek & Ekström, 1996) are shown in black. Red symbols show Helmholtz measurements that utilize the true station geometry at each array. For comparison, the Helmholtz measurements for the idealized 0.5º×0.5º station spacing are shown in blue, and green show measurements from the two-plane wave (TPW) inversion utilizing the phase and amplitude dataset for the true station geometry. The upward pointing black arrows at 20 s and 31 s indicate TPW measurements that plot beyond the vertical axis bounds ($\alpha \sim 26.9\times10^{-4}$ km^{-1} and 4.9×10^{-4} km^{-1}, respectively).

The 1-D attenuation coefficients measured from the real datasets are presented in Figure 9 for Nomelt (blue) and JdF (red). Attenuation is higher at JdF than NoMelt for periods < 70 s, whereas the opposite is true for periods > 90 s. To first order, our new observations at the two regions compare favorably with previous measurements using the TPW technique (lighter colored symbols in Figure 9), but important differences exist. Our observations show significantly higher attenuation at all periods at NoMelt and slightly lower attenuation on average at most periods at JdF. Attenuation at NoMelt is higher than PREM values at all periods > 30 s, whereas JdF shows much higher attenuation than PREM at periods < 80 s and comparable attenuation at periods > 80 s. Attenuation from global model QRFSI12 (Dalton et al., 2008; Dalton & Ekström, 2006) sampled within the NoMelt and JdF regions resembles the average behavior at > 50 s period, but differences in attenuation between the two regions are less pronounced than what we observe.

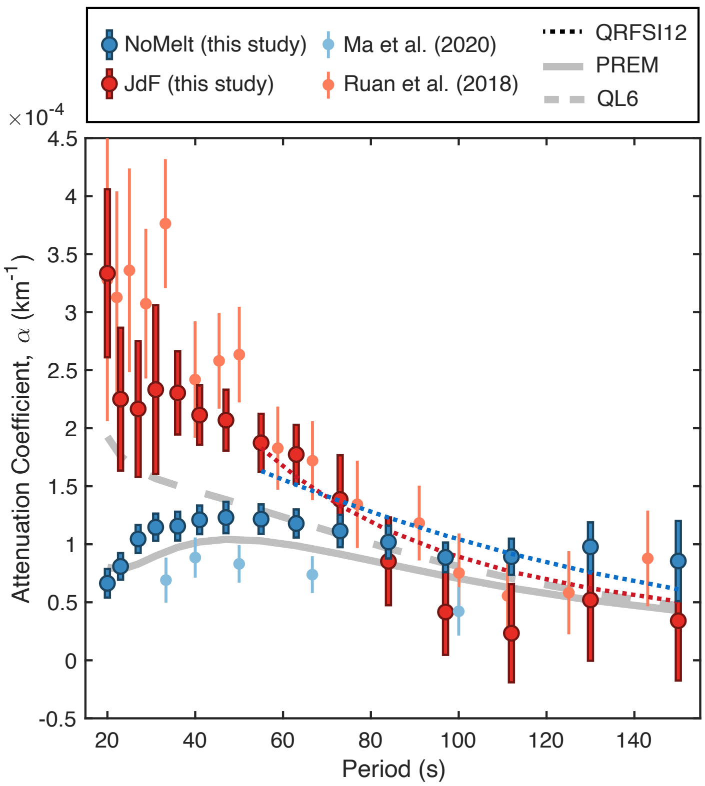

Figure 9. 1-D attenuation coefficients for periods ranging from 20–150 s for NoMelt (blue) and JdF (red). For comparison, TPW-derived estimates from two previous studies are shown for NoMelt (Ma et al., 2020) and JdF (Ruan et al., 2018). 1-D global models QL6 (Durek & Ekström, 1996) and PREM (Dziewonski & Anderson, 1981) are shown in gray. Dotted lines show attenuation from the 3-D global model QRFSI12 (Dalton et al., 2008) estimated at the center of each deployment location using MINEOS. Error bars represent 2σ uncertainty.

5.4 Shear attenuation profiles

We invert our new Helmholtz estimates of Rayleigh wave attenuation for profiles of upper mantle shear attenuation at NoMelt and JdF (Figure 10). Frequency-dependent Rayleigh wave attenuation, $Q^{-1}(\omega)$, is related to shear attenuation, $Q_\mu^{-1}(r)$, and bulk attenuation, $Q_\kappa^{-1}(r)$, as a function of radius r through the expression (Dziewonski & Anderson, 1981)

$$Q^{-1}(\omega) = \int_0^a \left[\, \mu(r)K_\mu(\omega,r)\, Q_\mu^{-1}(r) + \kappa(r)K_\kappa(\omega,r)\, Q_\kappa^{-1}(r)\, \right] dr \tag{14}$$

where μ and κ are the shear and bulk moduli, respectively, and K_μ and K_κ are the Fréchet kernels describing sensitivity of Rayleigh wave Q^{-1} to changes in Q_μ^{-1} and Q_κ^{-1}, respectively. Since both upper-mantle bulk attenuation and the sensitivity of Rayleigh waves to it are much smaller than is the case for shear attenuation, we fix Q_κ^{-1} to PREM values (Dziewonski & Anderson, 1981). We perform a regularized least-squares inversion of equation (14) for Q_μ^{-1} in the depth range 0–250 km with norm damping and second derivative smoothing, using MINEOS to calculate the sensitivity kernels (see Supplementary Figure S4). The sensitivity kernels primarily depend on the shear velocity structure, and therefore we first invert average phase velocity dispersion data for a smooth 1-D shear velocity profile at each location. We then invert for Q_μ^{-1} using the two-layer NoMelt attenuation model of Ma et al. (2020) as the starting model for both NoMelt and JdF, adjusting the water depth accordingly, but do not find a strong dependence on assumed starting model. Crustal Q_μ is held fixed at 1400. Model uncertainties are estimated through a bootstrap resampling approach in which the attenuation data are randomly perturbed within their uncertainty bounds and reinverted. This is repeated 500 times producing an ensemble of models, and the 1σ uncertainties are estimated from the middle 68% of the ensemble.

The resulting 1-D models of shear attenuation and their fit to the data are shown in Figure 10. Shear attenuation at NoMelt is characterized by a low attenuation lithospheric layer ($Q_\mu >$ 1500) overlying a high attenuation asthenospheric layer ($Q_\mu \sim$ 50–70) with a transition between the two occurring from ~50–100 km depth. At JdF, we observe a broad peak in attenuation ($Q_\mu \sim$ 50–60) centered at a depth of 100–130 km, bounded above and below by low attenuation regions ($Q_\mu >$ 200). In both cases, uncertainties increase with depth due to the larger uncertainties at longer periods.

6 Discussion

6.1 Advantages and limitations of Helmholtz tomography

We demonstrate that Helmholtz tomography can recover 1-D Rayleigh wave attenuation and 2-D maps of site amplification using typical OBS array geometries, even in the presence of strong elastic focusing and defocusing due to coastline effects. The power of the approach lies in its ability to account for complex patterns of elastic focusing without imposing strict physical assumptions about the nature of wavefield interference. Rather, the focusing behavior is directly observed and accounted for via $\nabla^2\tau$. In contrast, the TPW approach imposes a physical limitation on wavefield complexity. This approximation is sufficient in many settings, such as structurally homogeneous regions of the ocean basins far away from continents like NoMelt, but it may break down in more complex areas such as JdF, where the coastline has a large influence on multipathing behavior at periods < 35 s (Figure 8b). On the other hand, an important limitation of Helmholtz tomography is that it requires decent station coverage in two dimensions in order to accurately resolve the gradient and Laplacian fields in equation (6). Sharp lateral variations in these fields are challenging to resolve given the smooth regularization scheme used (equation (10)) and/or limitations in station coverage. In situations where station coverage is lacking, the TPW approach may be advantageous as the assumption of two interfering plane waves provides a solid physical basis for extrapolating wavefield behavior across data-poor regions.

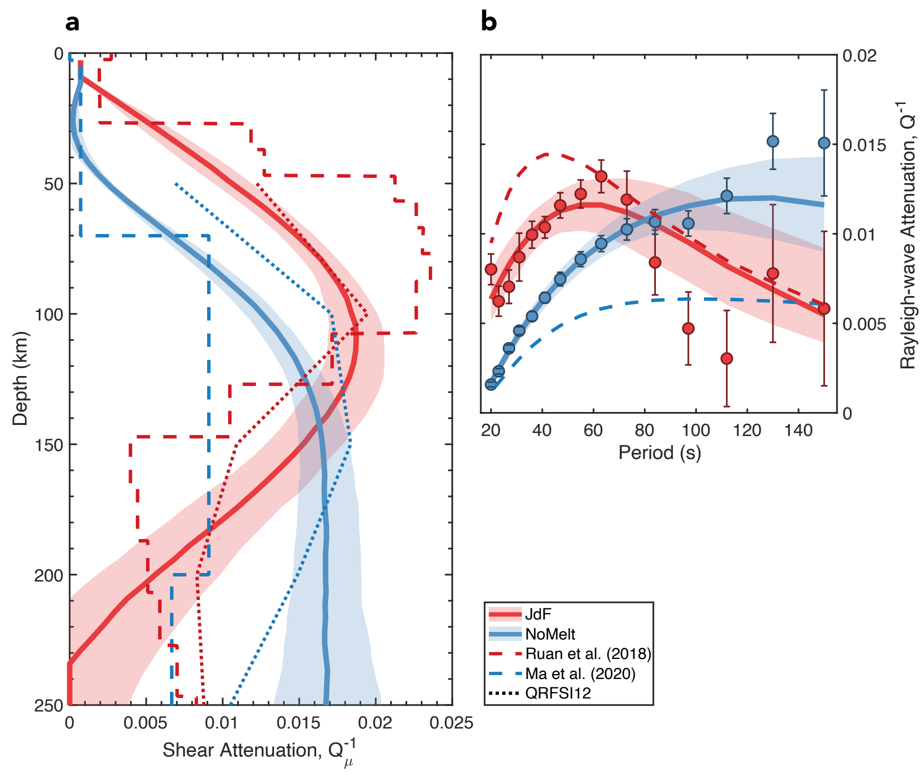

Figure 10. (a) Inversion for 1-D shear attenuation profiles at NoMelt (blue) and JdF (red). The solid lines and shaded regions show the median and 68% confidence interval, respectively, from bootstrap resampling. (b) Model fit to our data (filled circles with 1σ error bars). Previous 1-D shear attenuation models and predictions for NoMelt (Ma et al., 2020) and JdF (Ruan et al., 2018) are shown by dashed lines. Dotted lines show attenuation profiles from global model QRFSI12 (Dalton et al., 2008) extracted from the approximate deployment locations.

Helmholtz tomography is able to simultaneously account for both attenuation and site amplification via the mean and azimuthal variation of apparent amplitude decay, respectively. Accounting for local site amplification when estimating attenuation is especially important if amplification variations are strong and/or azimuthal gaps exist in the dataset. Both sources of bias can be understood by considering the synthetic JdF dataset as an example (Figure 6a,e). Apparent attenuation varies strongly with azimuth, especially at 31 s, and thus a dataset dominated by waves that propagate to the northeast at 60º azimuth would lead to attenuation estimates at JdF that are biased low (even negative), whereas the opposite would be true of a dataset dominated by waves propagating to the southwest at 240º. Such biases will increase with the magnitude of amplification variations (compare Figure 6a and 6e). Therefore, a decent azimuthal distribution of teleseismic earthquakes is necessary to prevent tradeoffs between attenuation and site amplification, especially if amplification variations are strong.

In this study, we focus on characterizing the average Rayleigh wave attenuation within small seismic arrays. Solving for 2-D maps of Rayleigh wave attenuation is desirable but challenging due to the issues outlined above, such as limited station coverage and potential tradeoffs due to uneven azimuthal distribution of earthquakes. Indeed, previous studies that utilized data from the USArray encountered challenges resolving detailed 2-D attenuation maps (F. C. Lin et al., 2012) and required both masking and spatial smoothing up to ~3º radius (Bao et al., 2016). Such smoothing would effectively smear away any lateral variation within a typical OBS array on the order of ~500x500 km^2. We therefore focus on 1-D array-average estimates of attenuation. As OBS arrays are typically small, 1-D attenuation is useful for characterizing OBS deployment regions. Although we focus here on applications to smaller scale OBS arrays, the methodology can be extended to similarly sized arrays in continental settings. For larger arrays such as the USArray, one could estimate 1-D attenuation within "subarrays" representing regions that are expected to contain little lateral heterogeneity. Additional synthetic testing using realistic wave propagation through laterally varying 3-D anelastic media is required to evaluate the ability to reliably resolve lateral variations in Rayleigh wave attenuation within larger arrays.

6.2 Comparison to previous attenuation studies

While our new observations of shear attenuation at NoMelt and JdF broadly resemble previous observations, important differences do exist. The approximate two-layer structure that we observe at NoMelt with a transition from low to high attenuation at 50–100 km depth is consistent with the two-layer model of Ma et al. (2020) with the lithosphere-asthenosphere boundary at 70 km depth; however, in the earlier study the asthenospheric layer shows lower attenuation ($Q_\mu \sim 110$) than we find here ($Q_\mu \sim$ 50–70), which underpredicts our Rayleigh wave attenuation observations at periods > 25 s (blue dashed line in Figure 10b). Compared to the NoMelt region in global model QRFSI12 (Dalton et al., 2008), our NoMelt model is slightly less attenuating from 50–150 km and is slightly more attenuating from 200–250 km. However, the general agreement is exceptional given the broad sensitivities associated with global modeling compared to our local estimates.

The high attenuation peak at 100–130 km depth that we observe at JdF resembles that of Ruan et al. (2018), but the attenuation peak in their model is both shallower (50–100 km) and stronger ($Q_\mu \sim 46$), overpredicting our attenuation observations for periods < 60 s (red dashed line in Figure 10b). The deeper high attenuation region in our model is more consistent with body-wave observations that imply a low viscosity melt column extending to ~150 km below the JdF Ridge (Eilon & Abers, 2017). The low attenuation region at >200 km depth in our model ($Q_\mu > 200$) appears less attenuating than Ruan et al. (2018) at first glance, but values are consistent to within uncertainty (see their Figure 2c). Our observations agree well with QRFSI12 at depths of 50–150 km, but we observe lower attenuation from 200–250 km.

Differences between our estimates of Q_μ at NoMelt and JdF and previous observations are primarily related to inconsistencies in the Rayleigh wave attenuation measurements (Figure 9), rather than in the inversion procedure. This point is demonstrated by the large misfit between previous model predictions of Rayleigh wave attenuation and our observations in Figure 10b. As the previous attenuation measurements of Ruan et al. (2018) and Ma et al. (2020) were made using the TPW method, a key question is whether these differences can be attributed to our use of Helmholtz tomography or whether they arise from the raw amplitude and/or phase measurements themselves. Our synthetic tests show that Helmholtz and TPW yield similar attenuation measurements (at periods >35 s, where focusing corrections are smaller), when applied to the same amplitude and phase dataset (Figure 8). A similar result is found using the real data: Helmholtz and TPW attenuation measurements agree to within uncertainty when applied to the same amplitude and phase dataset (pink symbols in Supplementary Figure S3). This suggests, albeit indirectly, that differences in our revised attenuation estimates arise from differences in the raw single-station amplitude measurements and/or event distribution and not the chosen theoretical framework used to interpret these amplitudes in terms of attenuation (i.e., Helmholtz versus TPW). We use the cross-correlation based ASWMS tool of Jin & Gaherty (2015) to measure station amplitude and differential phase, while previous TPW studies used a single-station Fourier transform (FT) based method (Forsyth & Li, 2005) to measure amplitude and phase. Both techniques involve time windowing and narrow-band filtering of the waveform, but windowing in ASWMS is performed automatically based on broadband Rayleigh wave energy (narrow-band filtering occurs after cross-correlation), whereas in the FT method, narrow-band filters are applied before windowing and user input is required to manually select the edges of each window. Given these differences, it is difficult to determine at what stage in the measurement procedures the amplitude measurements might diverge. We emphasize that phase velocity measurements using ASWMS and FT are equivalent to within uncertainty (see Figure 4a in Ma et al., 2020), indicating that phase is consistent between the two measurement techniques.

Both the Helmholtz and TPW methods applied to ASWMS amplitude and phase measurements are able to recover the true attenuation (and amplification) values from realistic SPECFEM3D GLOBE synthetic seismograms, providing confidence in our revised attenuation estimates at JdF and NoMelt. An advantage of our study is that we treat the JdF and NoMelt datasets identically throughout both the measurement and inversion procedures, and therefore, differences in attenuation observed between the two locations are driven by the data and not by ad hoc choices made within the analysis. In a future study, we will interpret these updated profiles of Q_μ alongside profiles of shear velocity to quantify temperature, melt fraction, and grain size in the oceanic asthenosphere.

6.3 Site amplification: A new observable in the oceans

Our observations of local site amplification, β, at JdF and NoMelt are among the first of their kind in an oceanic setting. Only a handful of previous studies have measured Rayleigh wave amplification at periods > 20 s (Bao et al., 2016; Bowden et al., 2017; Eddy & Ekström, 2014, 2020; F. C. Lin et al., 2012), and these studies all used data from the USArray. One study that we are aware of has inverted Rayleigh wave amplification measurements for shear velocity structure, and this too was carried out in the western U.S. (Schardong et al., 2019). The sensitivities of Rayleigh wave amplification to shear velocity (V_S), compressional velocity (V_P), and density (ρ) are complementary to that of phase velocity and may be used to refine models of 3-D Earth structure (Bowden et al., 2017; F. C. Lin et al., 2012; Schardong et al., 2019). Amplification displays opposite sensitivities to shear and compressional velocities at shallow depths, implying that V_P/V_S may be especially well resolved by amplification measurements (F. C. Lin et al., 2012). In contrast to phase and group velocity, the amplification sensitivity kernels for V_S have multiple zero-crossings and therefore should better resolve sharp gradients in shear velocity with depth (Babikoff, 2022; Dalton & Babikoff, 2021; F. C. Lin et al., 2012).

Our synthetic recovery tests (Figures 5 & 6) and application to the real datasets (Figure 7) demonstrate that amplification can be measured at typical OBS array geometries using Helmholtz tomography. Strong amplification observed along the JdF Ridge approximately coincides with slow phase velocities (Figure 4f), indicating that they can be inverted together to refine shallow Earth structure. In particular, improved shallow estimates of V_P/V_S at the JdF Ridge could shed light on the organization of melt and crustal accretion processes as well as shallow cracks and hydrothermal circulation (Kim et al., 2019; Lee et al., 2017; Takei, 2002). We reemphasize that β is a relative quantity with mean value equal to one within the array, and thus, an inversion of amplification for structural parameters V_S, V_P, and ρ must also preserve the array average. Joint inversion of amplification and phase velocity maps for crust and mantle properties at JdF will be the topic of a future study.

7 Conclusions

This manuscript demonstrates the first application of Helmholtz attenuation tomography in an oceanic setting, yielding new measurements of Rayleigh wave attenuation and local site amplification at 20–150 s period at the NoMelt and JdF regions. Using realistic simulations of wave propagation through 3-D elastic structure, we show that the technique faithfully accounts for wavefield focusing and defocusing, including in extreme scenarios associated with coastline effects. The focusing and defocusing corrections measured using the real dataset are qualitatively similar to that of the synthetics but are larger in amplitude, likely due to the smooth global model used to generate the synthetic dataset. The methodology has been implemented as an add-on to the ASWMS software package (Jin & Gaherty, 2015; see Open Research statement), offering a new tool for estimating Rayleigh wave attenuation and amplification across regional-scale arrays that has been validated using realistic synthetic seismograms. Although our focus is on applications at smaller scale OBS arrays (~500x500 km^2), the technique can be extended to comparable datasets on land.

Both 1-D attenuation and 2-D site amplification are successfully recovered in the synthetic tests at NoMelt and JdF, indicating that the array geometries and earthquake distributions are sufficient for resolving tradeoffs between attenuation and site amplification. When applied to the real data, our measurements of Rayleigh wave attenuation at NoMelt and JdF revise previous estimates derived using the TPW method. Our preliminary inversions of Rayleigh wave attenuation for 1-D profiles of shear attenuation, Q_μ, reveal significantly higher attenuation in the asthenosphere at NoMelt and a deeper high-attenuation region at JdF compared to previous studies. Maps of site amplification at JdF show high amplification (> 10% at 31 s period) along the low-velocity JdF Ridge, providing a new observable that can be inverted alongside phase velocity to improve models of shallow subsurface structure at the mid-ocean ridge.

Acknowledgments

The authors thank the science parties, captain and crew, and OBS instrument centers at WHOI, SIO, and LDEO who made possible the collection of the data used in this article. We thank Zhitu Ma and Donald Forsyth for insightful discussions regarding the two-plane wave method and

Helen Janiszewski for sharing Juan de Fuca plate boundary data. Finally, we thank Ge Jin and James Gaherty for developing and openly sharing/maintaining the ASWMS software, which was central to this study (see Open Research statement for the link to our modified ASWMS-Q code). This work was supported by an NSF EAR Postdoctoral Fellowship awarded to Russell (EAR-1952702).

Open Research

The methodology described in this manuscript is implemented as an add-on to the MATLAB-based Automated Surface-Wave Measurement System (ASWMS) and is hosted on GitHub (https://github.com/jbrussell/ASWMS-Q.git); the Mapping Toolbox is required. The maps in Figure 1 were generated using the Python-based PyGMT software (https://www.pygmt.org/). The SPECFEM3D_GLOBE software used to generate the synthetic datasets can be downloaded here: https://github.com/geodynamics/specfem3d_globe.git. The Automated Tilt and Compliance Removal (ATaCR) software can be accessed here: https://github.com/helenjanisz/ATaCR.git. Data used in this manuscript were retrieved from the Incorporated Research Institutions for Seismology (IRIS) Data Management Center (DMC) under network codes ZA (NoMelt) and 7D (Cascadia Initiative; Juan de Fuca).

References

Adenis, A., Debayle, E., & Ricard, Y. (2017a). Attenuation tomography of the upper mantle. *Geophysical Research Letters*, *44*, 7715–7724. https://doi.org/10.1002/2017GL073751

Adenis, A., Debayle, E., & Ricard, Y. (2017b). Seismic evidence for broad attenuation anomalies in the asthenosphere beneath the Pacific Ocean. *Geophysical Journal International*, *209*, 1677–1698. https://doi.org/10.1093/gji/ggx117

Babikoff, J. (2022). *Imaging the lithosphere and asthenosphere beneath North America with Rayleigh wave phase velocity and amplification*. Brown University.

Bao, X., Dalton, C. A., Jin, G., Gaherty, J. B., & Shen, Y. (2016). Imaging Rayleigh wave attenuation with USArray. *Geophysical Journal International*, *206*(1), 241–259. https://doi.org/10.1093/gji/ggw151

Bassin, C., Laske, G., & Masters, G. (2000). The Current Limits of Resolution for Surface Wave Tomography in North America. *EOS Trans AGU*, *81*, F897.

Bell, S. W., Ruan, Y., & Forsyth, D. W. (2016). Ridge asymmetry and deep aqueous alteration at the trench observed from Rayleigh wave tomography of the Juan de Fuca plate. *Journal of Geophysical Research : Solid Earth*, *121*, 7298–7321.

https://doi.org/10.1002/2016JB012990.Received

Bowden, D. C., Tsai, V. C., & Lin, F. C. (2017). Amplification and Attenuation Across USArray Using Ambient Noise Wavefront Tracking. *Journal of Geophysical Research: Solid Earth*, *122*, 10,086-10,101. https://doi.org/10.1002/2017JB014804

Byrnes, J. S., Toomey, D. R., Hooft, E. E. E., Nábělek, J., & Braunmiller, J. (2017). Mantle dynamics beneath the discrete and diffuse plate boundaries of the Juan de Fuca plate: Results from Cascadia Initiative body wave tomography. *Geochemistry, Geophysics, Geosystems*, *18*, 2906–2929. https://doi.org/10.1002/2017GC006980

Chevrot, S., & Lehujeur, M. (2022). Eikonal surface wave tomography with smoothing splines—application to Southern California. *Geophysical Journal International*, *229*(3), 1927–1941. https://doi.org/10.1093/gji/ggac034

Crawford, W. C., & Webb, S. C. (2000). Identifying and Removing Tilt Noise from Low Frequency (<0.1 Hz) Seafloor Vertical Seismic Data. *Bulletin of the Seismological Society of America*, *90*(4), 952–963. https://doi.org/10.1785/0119990121

Dalton, C. A., & Babikoff, J. (2021). Rayleigh wave amplification: sensitivity to elastic structure and application to Alaskan crust and upper mantle. In *AGU Fall Meeting Abstracts*. New Orleans.

Dalton, C. A., & Ekström, G. (2006). Global models of surface wave attenuation. *Journal of Geophysical Research: Solid Earth*, *111*(5), 1–19. https://doi.org/10.1029/2005JB003997

Dalton, C. A., & Faul, U. H. (2010). The oceanic and cratonic upper mantle: Clues from joint interpretation of global velocity and attenuation models. *Lithos*, *120*, 160–172. https://doi.org/10.1016/j.lithos.2010.08.020

Dalton, C. A., Ekström, G., & Dziewonski, A. M. (2008). The global attenuation structure of the upper mantle. *Journal of Geophysical Research*, *113*, 1–24. https://doi.org/10.1029/2007JB005429

Debayle, E., Bodin, T., Durand, S., & Ricard, Y. (2020). Seismic evidence for partial melt below tectonic plates. *Nature*, *586*, 555–559. https://doi.org/10.1038/s41586-020-2809-4

Durek, J. J., & Ekström, G. (1996). A radial model of anelasticity consistent with long-period surface-wave attenuation. *Bulletin of the Seismological Society of America*, *86*, 144–158.

Dziewonski, A. M., & Anderson, D. L. (1981). Preliminary reference Earth model. *Physics of the Earth and Planetary Interiors*, *25*, 297–356.

Eddy, C. L., & Ekström, G. (2014). Local amplification of Rayleigh waves in the continental United States observed on the USArray. *Earth and Planetary Science Letters*, *402*, 50–57. https://doi.org/10.1016/j.epsl.2014.01.013

Eddy, C. L., & Ekström, G. (2020). Comparisons between measurements and predictions of Rayleigh wave amplification across the contiguous United States. *Physics of the Earth and Planetary Interiors*, *299*, 106407. https://doi.org/10.1016/j.pepi.2019.106407

Eilon, Z. C., & Abers, G. A. (2017). High seismic attenuation at a mid-ocean ridge reveals the distribution of deep melt. *Science Advances*, *3*, e1602829. https://doi.org/10.1126/sciadv.1602829

Eilon, Z. C., & Forsyth, D. W. (2020). Depth-Dependent Azimuthal Anisotropy Beneath the Juan de Fuca Plate System. *Journal of Geophysical Research: Solid Earth*, *125*, e2020JB019477. https://doi.org/10.1029/2020JB019477

Ekström, G., Nettles, M., & Dziewoński, A. M. (2012). The global CMT project 2004-2010: Centroid-moment tensors for 13,017 earthquakes. *Physics of the Earth and Planetary Interiors*, *200–201*, 1–9. https://doi.org/10.1016/j.pepi.2012.04.002

Faul, U. H., & Jackson, I. (2005). The seismological signature of temperature and grain size variations in the upper mantle. *Earth and Planetary Science Letters*, *234*, 119–134. https://doi.org/10.1029/2001jb001225

Forsyth, D. W., & Li, A. (2005). Array Analysis of Two-Dimensional Variations in Surface Wave Phase Velocity and Azimuthal Anisotropy in the Presence of Multipathing Interference. *Seismic Earth: Array Analysis of Broadband Seismograms Geophysical Monograph Series*, *157*, 81–97.

Hariharan, A., Dalton, C. A., Ma, Z., & Ekström, G. (2020). Evidence of Overtone Interference in Fundamental-Mode Rayleigh Wave Phase and Amplitude Measurements. *Journal of Geophysical Research: Solid Earth*, *125*, 1–17. https://doi.org/10.1029/2019JB018540

Hariharan, A., Dalton, C. A., Babikoff, J., & Ekström, G. (2022). Controls on surface wave overtone interference. *Geophysical Journal International*, *228*, 1665–1683. https://doi.org/10.1093/gji/ggab424

Havlin, C., Holtzman, B. K., & Hopper, E. (2021). Inference of thermodynamic state in the asthenosphere from anelastic properties, with applications to North American upper mantle. *Physics of the Earth and Planetary Interiors*, *314*, 106639. https://doi.org/10.1016/j.pepi.2020.106639

Hawley, W. B., Allen, R. M., & Richards, M. A. (2016). Tomography reveals buoyant asthenosphere accumulating beneath the Juan de Fuca plate. *Science*, *353*(6306), 1406–1408. https://doi.org/10.1126/science.aad8104

Jackson, I., & Faul, U. H. (2010). Grainsize-sensitive viscoelastic relaxation in olivine: Towards a robust laboratory-based model for seismological application. *Physics of the Earth and Planetary Interiors*, *183*, 151–163. https://doi.org/10.1016/j.pepi.2010.09.005

Janiszewski, H. A., Gaherty, J. B., Abers, G. A., Gao, H., & Eilon, Z. C. (2019). Amphibious surface-wave phase-velocity measurements of the Cascadia subduction zone. *Geophysical Journal International*, *217*(3), 1929–1948. https://doi.org/10.1093/gji/ggz051

Jin, G., & Gaherty, J. B. (2015). Surface wave phase-velocity tomography based on multichannel cross-correlation. *Geophysical Journal International*, *201*(3), 1383–1398. https://doi.org/10.1093/gji/ggv079

Karaoğlu, H., & Romanowicz, B. (2018). Inferring global upper-mantle shear attenuation structure by waveform tomography using the spectral element method. *Geophysical Journal International*, *213*, 1536–1558. https://doi.org/10.1093/gji/ggy030

Kim, E., Toomey, D. R., Hooft, E. E. E., Wilcock, W. S. D., Weekly, R. T., Lee, S. M., & Kim, Y. H. (2019). Upper Crustal Vp/Vs Ratios at the Endeavour Segment, Juan de Fuca Ridge, From Joint Inversion of P and S Traveltimes: Implications for Hydrothermal Circulation.

Geochemistry, Geophysics, Geosystems, *20*, 208–229. https://doi.org/10.1029/2018GC007921

Komatitsch, D., & Tromp, J. (2002a). Spectral-element simulations of global seismic wave propagation—II. Three-dimensional models, oceans, rotation and self-gravitation. *Geophysical Journal International*, *150*, 303–318. https://doi.org/10.1046/j.1365-246X.2002.01653.x

Komatitsch, D., & Tromp, J. (2002b). Spectral-element simulations of global seismic wave propagation - I. Validation. *Geophysical Journal International*, *149*(2), 390–412. https://doi.org/10.1046/j.1365-246X.2002.01653.x

Kustowski, B., Ekstro, G., & Dziewonski, A. M. (2008). Anisotropic shear-wave velocity structure of the Earth's mantle: A global model. *Journal of Geophysical Research*, *113*, 1–23. https://doi.org/10.1029/2007JB005169

Langston, C. A. (2007a). Spatial gradient analysis for linear seismic arrays. *Bulletin of the Seismological Society of America*, *97*(1 B), 265–280. https://doi.org/10.1785/0120060100

Langston, C. A. (2007b). Wave gradiometry in the time domain. *Bulletin of the Seismological Society of America*, *97*(3), 926–933. https://doi.org/10.1785/0120060152

Langston, C. A. (2007c). Wave gradiometry in two dimensions. *Bulletin of the Seismological Society of America*, *97*(2), 401–416. https://doi.org/10.1785/0120060138

Lee, A. L., Walker, A. M., Lloyd, G. E., & Torvela, T. (2017). Geochemistry, Geophysics, Geosystems. *Geochemistry, Geophysics, Geosystems*, *18*, 1090–1110. https://doi.org/10.1002/2016GC006705.Received

Lin, F.-C., & Ritzwoller, M. H. (2011). Helmholtz surface wave tomography for isotropic and azimuthally anisotropic structure. *Geophysical Journal International*, *186*(3), 1104–1120. https://doi.org/10.1111/j.1365-246X.2011.05070.x

Lin, F.-C., Ritzwoller, M. H., & Snieder, R. (2009). Eikonal tomography: surface wave tomography by phase front tracking across a regional broad-band seismic array. *Geophysical Journal International*, *177*(3), 1091–1110. https://doi.org/10.1111/j.1365-246X.2009.04105.x

Lin, F. C., Tsai, V. C., & Ritzwoller, M. H. (2012). The local amplification of surface waves: A new observable to constrain elastic velocities, density, and anelastic attenuation. *Journal of Geophysical Research: Solid Earth*, *117*(6), 1–20. https://doi.org/10.1029/2012JB009208

Lin, P.-Y. P., Gaherty, J. B., Jin, G., Collins, J. A., Lizarralde, D., Evans, R. L., & Hirth, G. (2016). High-resolution seismic constraints on flow dynamics in the oceanic asthenosphere. *Nature*, *535*(7613), 1–9. https://doi.org/10.1038/nature18012

Liu, H., Anderson, D. L., & Kanamori, H. (1976). Velocity dispersion due to anelasticity; implications for seismology and mantle composition. *Geophysical Journal of the Royal Astronomical Society*, *47*, 41–58. https://doi.org/10.1111/j.1365-246X.1976.tb01261.x

Liu, Y., & Holt, W. E. (2015). Wave gradiometry and its link with Helmholtz equation solutions applied to USArray in the eastern U.S. *Journal of Geophysical Research: Solid Earth*, *120*, 5717–5746. https://doi.org/10.1002/2015JB011982

Ma, Z., Dalton, C. A., Russell, J. B., Gaherty, J. B., Hirth, G., & Forsyth, D. W. (2020). Shear attenuation and anelastic mechanisms in the central Pacific upper mantle. *Earth and Planetary Science Letters*, *536*, 116148. https://doi.org/10.1016/j.epsl.2020.116148

Mark, H. F., Lizarralde, D., Collins, J. A., Miller, N. C., Hirth, G., Gaherty, J. B., & Evans, R. L. (2019). Azimuthal Seismic Anisotropy of 70-Ma Pacific-Plate Upper Mantle. *Journal of Geophysical Research: Solid Earth*, *124*, 1889–1909. https://doi.org/10.1029/2018JB016451

Mark, H. F., Collins, J. A., Lizarralde, D., Hirth, G., Gaherty, J. B., Evans, R. L., & Behn, M. D. (2021). Constraints on the Depth, Thickness, and Strength of the G Discontinuity in the Central Pacific From S Receiver Functions. *Journal of Geophysical Research: Solid Earth*, *126*, e2019JB019256. https://doi.org/10.1029/2019JB019256

McCarthy, C., & Takei, Y. (2011). Anelasticity and viscosity of partially molten rock analogue: Toward seismic detection of small quantities of melt. *Geophysical Research Letters*, *38*(18), 3–7. https://doi.org/10.1029/2011GL048776

McCarthy, C., Takei, Y., & Hiraga, T. (2011). Experimental study of attenuation and dispersion over a broad frequency range: 2. the universal scaling of polycrystalline materials. *Journal of Geophysical Research: Solid Earth*, *116*(9), 1–18. https://doi.org/10.1029/2011JB008384

Priestley, K., & McKenzie, D. (2013). The relationship between shear wave velocity, temperature, attenuation and viscosity in the shallow part of the mantle. *Earth and Planetary Science Letters*, *381*, 78–91. https://doi.org/10.1016/j.epsl.2013.08.022

Richards, F. D., Hoggard, M. J., White, N., & Ghelichkhan, S. (2020). Quantifying the Relationship Between Short-Wavelength Dynamic Topography and Thermomechanical Structure of the Upper Mantle Using Calibrated Parameterization of Anelasticity. *Journal of Geophysical Research: Solid Earth*, *125*(9). https://doi.org/10.1029/2019JB019062

Ruan, Y., Forsyth, D. W., & Bell, S. W. (2018). Shear attenuation beneath the Juan de Fuca plate: Implications for mantle flow and dehydration. *Earth and Planetary Science Letters*, *496*, 189–197. https://doi.org/10.1016/j.epsl.2018.05.035

Russell, J. B., & Gaherty, J. B. (2021). Lithosphere Structure and Seismic Anisotropy Offshore Eastern North America: Implications for Continental Breakup and Ultra-Slow Spreading Dynamics. *Journal of Geophysical Research: Solid Earth*, *126*, e2021JB022955. https://doi.org/10.1029/2021JB022955

Russell, J. B., Gaherty, J. B., Lin, P.-Y. P., Lizarralde, D., Collins, J. A., Hirth, G., & Evans, R. L. (2019). High-Resolution Constraints on Pacific Upper Mantle Petrofabric Inferred From Surface-Wave Anisotropy. *Journal of Geophysical Research: Solid Earth*, *124*(1). https://doi.org/10.1029/2018JB016598

Saikia, U., Rychert, C. A., Harmon, N., & Michael Kendall, J. (2021). Seismic Attenuation at the Equatorial Mid-Atlantic Ridge Constrained by Local Rayleigh Wave Analysis From the PI-LAB Experiment. *Geochemistry, Geophysics, Geosystems*, *22*, 1–16. https://doi.org/10.1029/2021GC010085

Sarafian, E., Evans, R. L., Collins, J. a, Elsenbeck, J., Gaetani, G. a, Gaherty, J. B., et al. (2015). The electrical structure of the central Pacific upper mantle constrained by the NoMelt experiment. *G3*, *16*, 1115–1132. https://doi.org/10.1002/2014GC005709.Received

Schardong, L., Ferreira, A. M. G., Berbellini, A., & Sturgeon, W. (2019). The anatomy of uppermost mantle shear-wave speed anomalies in the western U.S. from surface-wave amplification. *Earth and Planetary Science Letters*, *528*, 115822. https://doi.org/10.1016/j.epsl.2019.115822

Seton, M., Müller, R. D., Zahirovic, S., Williams, S., Wright, N. M., Cannon, J., et al. (2020). A Global Data Set of Present-Day Oceanic Crustal Age and Seafloor Spreading Parameters. *Geochemistry, Geophysics, Geosystems*, *21*, e2020GC009214. https://doi.org/10.1029/2020GC009214

Takei, Y. (2002). Effect of pore geometry on Vp/Vs: From equilibrium geometry to crack. *Journal of Geophysical Research*, *107*(B2), 2043. https://doi.org/10.1029/2001jb000522

Tromp, J., & Dahlen, F. A. (1992). Variational Principles For Surface Wave Propagation On A Laterally Heterogeneous Earth-Iii. Potential Representation. *Geophysical Journal International*, *112*, 195–209. https://doi.org/10.1111/j.1365-246X.1993.tb01449.x

Webb, S. C., & Crawford, W. C. (1999). Long-period seafloor seismology and deformation under ocean waves. *Bulletin of the Seismological Society of America*, *89*(6), 1535–1542. https://doi.org/10.1785/bssa0890061535

Yamauchi, H., & Takei, Y. (2016). Polycrystal anelasticity at near-solidus temperatures. *Journal of Geophysical Research: Solid Earth*, *121*, 7790–7820. https://doi.org/10.1002/2016JB013316

Yang, Y., & Forsyth, D. W. (2006). Regional tomographic inversion of the amplitude and phase of Rayleigh waves with 2-D sensitivity kernels. *Geophysical Journal International*, *166*(3), 1148–1160. https://doi.org/10.1111/j.1365-246x.2006.02972.x